2016

Recruitment of inhibition and excitation across mouse visual cortex depends on the hierarchy of interconnecting areas

Rinaldo D. D'Souza
Washington University School of Medicine

Andrew M. Meier
Washington University School of Medicine

Pawan Bista
Washington University School of Medicine

Quanxin Wang
Washington University School of Medicine

Andreas Burkhalter
Washington University School of Medicine

Recruitment of inhibition and excitation across mouse visual cortex depends on the hierarchy of interconnecting areas

[1]Rinaldo D. D'Souza, [1]Andrew M. Meier, [1]Pawan Bista, [2]Quanxin Wang, [1]Andreas Burkhalter

[1]Department of Neuroscience, Washington University School of Medicine, St. Louis, Missouri, 63110; [2]Allen Institute for Brain Science, Seattle, Washington 98103

Correspondence:

Andreas Burkhalter PhD

Department of Neuroscience, 8108

Washington University School of Medicine

660 S. Euclid Avenue

St. Louis, MO 63110

Phone: (314) 362-4068

Fax: (314) 362-3446

E-mail: burkhala@wustl.edu

Abstract

Diverse features of sensory stimuli are selectively processed in distinct brain areas. The relative recruitment of inhibitory and excitatory neurons within an area controls the gain of neurons for appropriate stimulus coding. We examined how such a balance of inhibition and excitation is differentially recruited across multiple levels of a cortical hierarchy by mapping the locations and strengths of synaptic inputs to pyramidal and parvalbumin (PV)-expressing neurons in feedforward and feedback pathways interconnecting primary (V1) and two higher visual areas. While interareal excitation was stronger in PV than in pyramidal neurons in all layer 2/3 pathways, we observed a gradual scaling down of the inhibition/excitation ratio from the most feedforward to the most feedback pathway. Our results indicate that interareal gain control depends on the hierarchical position of the source and the target, the direction of information flow through the network, and the laminar location of target neurons.

.

Introduction

Visual perception and visually guided actions result from coordinated neuronal communication between multiple, functionally diverse areas of visual cortex. Within visual cortex, interareal communication is achieved through axons of pyramidal (Pyr) cells carrying feedforward (FF) information from lower to higher areas and feedback (FB) signals through 'top-down' connections descending across the hierarchy of visual areas[1,2]. How neurons within such a highly interconnected network and increasing densities of inputs at higher levels of the cortical hierarchy[3,4] maintain stimulus-specificity without saturating their spike output has been studied by modelling the effects of inhibitory synaptic inputs and by recording the balance of excitation and inhibition in local networks of sensory cortex[5,6]. However, the rules by which the inhibition/excitation (I/E) balance changes along processing pathways from early to deep stages of the brain and back are incompletely understood.

In the rodent visual system, interareal FF and FB pathways communicate through excitatory synapses contacting Pyr and GABAergic neurons[7]. In the target area, both cell types are reciprocally connected by a fine-scale circuit embedded within the global network[8-10]. Although interareal FF and FB connections terminate on multiple types of GABAergic neurons, most of them synapse onto PV-expressing fast-spiking interneurons[11-13], which provide feedforward inhibition (FFI) to local Pyr cells[14,15].

FFI is a common functional motif throughout the brain, capable of regulating the I/E balance and thereby influencing the gain, the integration window, and the temporal precision of inputs[5,16-18]. Similar to the thalamocortical and local circuits in mouse barrel cortex and in V1[16,17], FFI is also involved in interareal communication across the visual cortical hierarchy[14]. In fact, our studies in mouse visual cortex have shown that FF input to Pyr cells is more strongly counterbalanced by inhibition than FB input, suggesting pathway-specific differences in the gain and dynamic range of recurrent excitation involved in cortical computations[15,16,19].

Here, we demonstrate that higher relative inhibition in FF than in FB pathways is part of a more general rule of cortico-cortical communication. We studied the strengths of FF and FB inputs interconnecting mouse V1 with Pyr and PV neurons in the extrastriate area PM (posteromedial) situated high in the hierarchy, and compared the I/E balance with input to and from the hierarchically intermediate area LM (lateromedial). Using whole-cell patch clamp recordings and laser-scanning photostimulation of Channelrhodopsin-2 (ChR2)-expressing FF and FB connections in acute cortical slices, we show that the relative strength of excitatory input to Pyr and PV cells is pathway-specific and depends on the position of the source and target areas within the hierarchy. Interareal inputs to PV interneurons in upper layers, but not in lower layers, are stronger than to Pyr cells, and the asymmetry of I/E balance was greater for V1 to PM than for LM to PM connections, suggesting weaker FFI by inputs from hierarchically higher areas. In support of the notion that pathways from sources deeper in the brain, which deliver input that vary over a narrower range than input from the outside world, would require lower levels of inhibitory control, we found that FFI is weaker in FB connections and weakest in FB input to V1, at the bottom of the hierarchy. Our findings therefore suggest that in FF and FB pathways targeting neurons in layer 2/3 (L2/3), excitation is more strongly counterbalanced by inhibition and that the imbalance is gradually rectified according to hierarchical distance from the most feedforward to the most feedback.

Results

Hierarchy between V1, LM and PM

To study interareal inhibition across different levels of the cortical architecture we first asked whether the visual areas V1, LM and PM lie at distinct levels of an interconnected hierarchical network. To do this we traced the outputs from V1, LM and PM with the anterograde tracer biotinylated dextran amine (BDA) and studied the laminar patterns of axon terminals in

each of the visual cortical target areas: V1, LM, POR (postrhinal), AL (anterolateral), P (posterior), LI (laterointermediate), PM, AM (anteromedial), RL (rostrolateral) and A (anterior) (Figure 1, Figure 1 – figure supplement 1-3). Projections were assigned to areas by their locations relative to retrogradely bisbenzimide-labeled callosal landmarks[20], which we imaged *in situ* before sectioning the brain, and by their relative positions to each other (Figure 1a). Sections were numbered from the posterior pole of cortex so that the callosal landmarks seen in the coronal plane could be matched to specific locations of the *in situ* pattern. BDA labeled fibers were then superimposed onto the callosal pattern observed in the same section, and projections were assigned to specific areas according to the map by Wang and Burkhalter[20] (Figure 1a). Optical density maps of projections showed striking laminar differences (Figure 1b). Although most projections involved L1-6, inputs from V1 consistently showed dense terminations in L2-4 of each of the higher areas with much sparser projections in L1. In contrast, projections from both LM and PM strongly targeted L1 of V1 while weakly targeting L2-4 (Figure 1 – figure supplement 2 and 3). The selective targeting of L1 by FB projections is consistent with observations in other species[1,2,21,22]. To analyze these patterns quantitatively, we computed the density ratio (DR) of terminations in L2-4 to that in L1 of axons from V1, LM and PM to each of the other nine areas and plotted DRs in a 3 x 9 matrix (Figure 1c). We reasoned that FF projections from lower areas would, on average, have a higher DR than FB projections from higher areas. The matrix showed that the average DRs in all targets of V1 were > 2.52 ± 0.31, whereas the DRs for projections to V1 were < 0.72 ± 0.08 (Figure 1c). Pairwise comparisons of average DRs of projections from each of V1, LM, and PM to the other areas showed significant ($p < 0.001$, Mann-Whitney U test) differences, demonstrating that V1, LM and PM are at distinct hierarchical levels, with LM at the intermediate level between V1 and PM (Figure 1d, e).

L2/3 FF and FB pathways between V1 and PM

Cortico-cortical inhibition between areas involves both, the initial excitation of interneurons by long-range axonal projections of Pyr cells, and the disynaptic inhibition of Pyr cells by interneurons. As a first step in the analysis of the recruitment of interareal inhibition, we first confirmed the role of PV interneurons in inhibiting neighboring Pyr cells. These experiments were performed in area PM, one of the targets of V1, in acute slices from mice in which PV cells expressed tdTomato (tdT) (Figure 2 – figure supplement 1a). The axonal projections from V1 to PM were labeled by anterograde tracing with adeno associated virus (AAV) expressing a ChR2-Venus fusion protein[23] (Figure 2 – figure supplement 1a-f). PM is the posterior projection zone medial to the densely type 2 muscarinic acetylcholine receptor (M2)-expressing area V1[24,25] (Figure 2 – figure supplement 1d, e). Similar to other cortical areas, PM contained tdT-PV cell bodies in L2-6, with axons and dendrites reaching into L1 (Figure 2 – figure supplement 1f, figure supplement 2a). We performed paired recordings to examine whether increasing the excitation of PV cells results in stronger inhibition of neighboring synaptically connected Pyr cells (Figure 2 – figure supplement 2c). To do this, we evoked action potentials by injecting current steps (100, 200, 300, and 400 pA; 50 ms; Figure 2 – figure supplement 2c-f) into PV cells and recorded inhibitory postsynaptic currents (IPSCs) in connected Pyr cells. Similar to recordings in other cortical areas[10,26] we found a high connection probability. Recordings from PV and Pyr neurons within ~100 µm of each other resulted in 11/13 (84.6%) and 7/15 (46.6%) synaptically connected pairs in L2/3 and L5, respectively (Figure – figure supplement 2g). In both layers, increasing the firing of PV cells resulted in larger IPSCs in Pyr cells (n = 11 pairs in L2/3, 7 pairs in L5; Figure 2 – figure supplement 2d-f). The increase in inhibition was due to both, the increased probability of PV cells to reach spike threshold, as well as increased spiking. These findings reveal a local subnetwork that is likely tapped by interareal connections for FFI of Pyr cells in target areas.

Because the level of PV cell excitation determines the feedforward inhibitory drive to synaptically connected Pyr cells, we examined the strength of excitatory inputs to neighboring PV and Pyr cells by different pathways. We performed subcellular ChR2-assisted circuit mapping (sCRACM)[15,23,27] in acute slices of visual cortex to measure the input strength and laminar location of interareal connections to PV and Pyr cells in different pathways. To study connections in the $FF_{V1\rightarrow PM}$ pathway, we expressed ChR2-Venus in axons projecting from V1 to PM, and recorded excitatory postsynaptic currents (EPSCs) from PV and Pyr cells centered at the peak of the PM projection (Figure 2a). Photostimulation of ChR2-expressing axon terminals was achieved by a 473 nm laser delivered one spot at a time in a grid pattern separated by 75 μm (Figure 2b). Recordings were performed in the presence of 1 μm TTX (tetrodotoxin) and 50 μm 4-AP (4-aminopyridine) in the bath to block polysynaptic currents and repolarization of axon terminals, respectively. Resulting EPSCs were measured by whole cell patch clamp recordings from PV and Pyr neurons voltage-clamped at -70 mV (Figure 2c). We compared EPSCs between PV and Pyr neurons whose cell bodies were in the same layer of the same slice, within ~100 μm of each other.

In the L2/3 $FF_{V1\rightarrow PM}$ pathway, EPSCs recorded from PV cells were larger than those from Pyr cells (Figure 2c-f). On average, the largest EPSCs were evoked from synaptic inputs to proximal dendrites at the bottom of L2/3 whereas inputs to distal dendrites were weaker (Figure 2d, e). The mean total current in PV cells was 12.85 ± 4.48-fold stronger than that in neighboring Pyr cells ($p < 0.001$, n = 14 pairs). To illustrate the relative excitation of PV and Pyr cells, we plotted the total EPSC in each PV cell against the total EPSC in its Pyr neighbor, and measured the mean slope for all such pairs in this pathway (Figure 2f). We also computed the mean slope after normalizing the EPSC to the mean cell conductance to control for cell size. Similar to observations in thalamocortical and local circuits, the time to peak of EPSCs was significantly shorter in PV than in Pyr cells (Figure 2g; n = 14 pairs, $p < 0.05$, paired t-test),

consistent with the notion that PV interneurons can be recruited more rapidly than Pyr neurons in diverse brain areas[28,29].

We next asked whether connections to PV and Pyr cells in the $FB_{PM\rightarrow V1}$ pathway showed a different I/E balance. Recordings in V1 showed that similar to PM, EPSCs in PV cells were larger and faster than in Pyr cells (Figure 3a-f). In contrast to the $FF_{V1\rightarrow PM}$ pathway, however, the excitation of PV cells in the $FB_{PM\rightarrow V1}$ pathway was only 1.93 ± 0.44-fold stronger than Pyr cell excitation. Thus, the excitation of PV cells, relative to that of neighboring Pyr cells, was weaker in the $FB_{PM\rightarrow V1}$ than in the $FF_{V1\rightarrow PM}$ pathway (Figure 3g; n = 14 pairs for $FF_{V1\rightarrow PM}$, n = 21 pairs for $FB_{PM\rightarrow V1}$; $p < 0.001$), similar to previous observations in the L2/3 $FF_{V1\rightarrow LM}$ and $FB_{LM\rightarrow V1}$ pathways[15]. The larger EPSCs in PV cells could be a result of either a higher density of excitatory input or due to a larger area over which individual PV cells are contacted by interareal projections, or both. We therefore measured the mean EPSC per pixel and the total area over which each cell type exhibited measurable EPSCs (Figure 3 – figure supplement 1). In the $FF_{V1\rightarrow PM}$ pathway, PV cells exhibited larger EPSCs per pixel than Pyr cells (Figure 3 – figure supplement 1a) as well as received input over a larger area (Figure 3 – figure supplement 1b). In contrast, in the $FB_{PM\rightarrow V1}$ pathway, the mean EPSC per pixel between the two cell types were not significantly different (Figure 3 – figure supplement 1c), indicating that the larger total EPSCs in PV cells were the result of PV cells receiving excitatory input over a larger area (Figure 3 – figure supplement 1d).

The laminar organization of interareal input to individual neurons was significantly different for the two pathways. Unlike $FF_{V1\rightarrow PM}$ projections, FB axons from PM provided strong inputs to L1 of V1. We quantified L1 input by measuring the total pixel values in each row of the photostimulation grid pattern and plotting EPSCs against distance from the pial surface (Figure 3h, i). The values are percentages in each row of the total EPSC in the respective cell type. Consistent with the distribution of projections (Figure 1b) the proportion of inputs to L1, relative

to total EPSCs, was larger in the $FB_{PM\rightarrow V1}$ pathway than in the $FF_{V1\rightarrow PM}$ pathway (Figure 3i; $p <$ 0.01 for both PV and Pyr cells). It must be noted, however, that due to dendritic filtering of signals, EPSCs at distal dendrites are attenuated more than those near the soma. Thus, the proportion of L1 inputs to the total current may be an underestimate.

L2/3 FF and FB pathways between LM and PM

Do connections originating from higher areas follow the same normalization rules as those from V1? We addressed this question with sCRACM experiments in L2/3 of $FF_{LM\rightarrow PM}$ and $FB_{PM\rightarrow LM}$ pathways (Figure 4). Similar to FF and FB pathways between V1 and PM, EPSCs were larger in PV cells than in Pyr cells in both pathways (Figure 4a-f). In the $FF_{LM\rightarrow PM}$ pathway, the mean total current in PV cells was 3.62 ± 0.75-fold larger than in neighboring Pyr cells (n = 15 pairs, $p < 0.02$; Figure 4c, g). Inputs to both cell types were maximal at proximal dendrites in L3 and 4, but weak in L1 and L2 (Figure 4a, b, i; Figure 4 – figure supplement 1). In the $FB_{PM\rightarrow LM}$ pathway, the mean total EPSC to PV cells was 3.77 ± 0.81-fold the total EPSC in neighboring Pyr cells, with substantial input into L1 (n = 18 pairs, $p < 0.01$; Figure 4d-f, h, i; Figure 4 – figure supplement 1). Similar to connections between V1 and PM, EPSCs were faster in PV than in Pyr cells in both $FF_{LM\rightarrow PM}$ and $FB_{PM\rightarrow LM}$ pathways (Figure 4 – figure supplement 2d). Hence, the faster activation of PV cells appears to be a general rule for FFI provided by long-range connections[28,29].

While PV cells received stronger excitatory inputs than Pyr cells in all four L2/3 pathways described here, the difference in the relative excitation of PV and Pyr was bigger in the $FF_{V1\rightarrow PM}$ originating at the bottom and terminating at the top of the hierarchy than in the $FF_{LM\rightarrow PM}$ pathway originating from the higher area, LM (Figure 4g). In contrast, in the $FB_{PM\rightarrow V1}$ pathway, the difference was smaller for connections originating at the top and terminating at the bottom of the hierarchy than for terminations at an intermediate level in LM (Figure 4h). These relationships are evident in a significant ($p < 0.001$, Kruskal-Wallis test) decrease of the $EPSC_{PV}/EPSC_{Pyr}$

ratios, when pathways are ordered by hierarchical distance from the most feedforward to the most feedback (Figure 1e, 4j). The plot suggests that inhibitory counterbalance to long-range excitation is gradually adjusted depending on the hierarchical location of the source and target areas. Although the total input to PV and Pyr cells differed across pathways, the pathway-specific normalization was independent of the absolute strength of the excitatory input so that the $EPSC_{PV}/EPSC_{Pyr}$ ratios, and not the absolute values of EPSCs in PV and Pyr cells, show a hierarchy-dependent variation (Figure 4 – figure supplement 2a-c).

FF and FB pathways in L5

We next asked if interareal inputs to L5 neurons follow a similar physiological connectivity rule as those to L2/3. Unlike in L2/3, the EPSCs recorded in L5 PV and Pyr cells upon stimulation of $FF_{V1\rightarrow PM}$ and $FF_{LM\rightarrow PM}$ axons were not significantly different (Figure 5a-f). The relative excitation of L5 PV cells, expressed by the $EPSC_{PV}/EPSC_{Pyr}$ ratio, was smaller than that observed in L2/3 for both FF pathways (Figure 5g, h). While we did not observe EPSCs in L1 for L5 Pyr cells, likely due to attenuation of signals by dendritic filtering, we detected significant input to L2-4. In particular, L5 Pyr cells in $FF_{LM\rightarrow PM}$ exhibited large EPSCs at apical dendrites in L2-4, hundreds of microns distal to the cell body (Figure 5d, e, i, j). The proportion of such L2-4 inputs to the total EPSC was higher in $FF_{LM\rightarrow PM}$ than in $FF_{V1\rightarrow PM}$ for L5 Pyr cells but not for PV cells, whose input distributions were similar in both pathways (Figure 5i, j). Thus depending on the source of long-range synaptic input, L5 Pyr cells in PM receive FF input at different locations of their dendritic arbor.

Finally, we examined the two FB pathways projecting from PM to L5 neurons in V1 and LM respectively. Activation of either $FB_{PM\rightarrow V1}$ or the $FB_{PM\rightarrow LM}$ projecting axons resulted in EPSCs of similar magnitudes in neighboring PV and Pyr cells (Figure 6a-f), with the strongest inputs primarily recorded at proximal dendrites in L5 for both cell types (Figure 6g). These results suggest that the stronger activation of PV cells observed in L2/3 is absent in L5. Consistent with

this observation, we found no significant difference between the $EPSC_{PV}/EPSC_{Pyr}$ ratios for L5 cell pairs for the different pathways (Figure 6h), suggesting equal potency of FFI among these pathways regardless of whether they are FF or FB. Similar to L2/3, however, the EPSCs in PV cells showed faster rise times than those in Pyr cells in all L5 pathways (Figure 6i).

Discussion

We have mapped input strengths to inhibitory PV and excitatory Pyr cells in diverse pathways interconnecting three visual cortical areas with distinct spatiotemporal sensitivities and specialized functions[30-33]. The results in L2/3 support the notion that in FF and FB pathways, excitation is more strongly counterbalanced by inhibition and that the imbalance is gradually rectified according to hierarchical distance from the most FF to the most FB (Figure 1e, 4j). The results further suggest that the hierarchical distance rule of normalization is independent of the absolute magnitude of EPSCs across the hierarchy (Figure 4 – figure supplement 2a-c). Our findings argue that excitation ascending across multiple hierarchical levels is gradually adjusted to keep the dynamic range of L2/3 Pyr cell firing constant and compensate for the increased density of synaptic input to Pyr cells in higher cortical areas[4]. Strong activation of PV neurons may narrow the window for effective excitation and result in high frequency gamma-band synchronization of activity found in FF signaling[17,34,35]. In contrast, in FB pathways excitation is weakly counterbalanced by inhibition, which may broaden the window for synaptic integration and result in slower synchronization frequencies found in FB communications[35]. Thus, variation in I/E balance, through the differential recruitment of PV and Pyr neurons in different cortical pathways, is a key feature of distributed hierarchical processing.

Reciprocal connections between areas are a highly conserved feature of mammalian cortex. However, the exact pattern of termination of FF and FB axonal projections in the target area appears to vary between species, particularly in the termination patterns of FF pathways in layers 2, 3 and 4[1,36,37]. Despite these differences, a consistent observation among different

266 species is a tendency for FF projections to avoid L1 and the selective targeting of L1 by FB
267 pathways[2,21,22,38]. We therefore used the average DR of axonal terminations in L2-4 to those in
268 L1 to classify pathways on a sliding scale as being FF or FB. In this reference frame, V1, LM
269 and PM constitute a clear hierarchy, which broadly matches that of rat visual cortex[2] and is
270 consistent with the increasing size of receptive fields[20]. The hierarchical ordering of V1, LM and
271 PM based on average DRs is consistent with the ordering based on the difference of DRs
272 between reciprocally connected pairs. This is notable because differences in the laminar
273 patterns of reciprocal projections between two areas have traditionally been used to arrange
274 areas in a hierarchy[1,2]. While our method of averaging DRs provides a hierarchy based on how
275 individual visual areas project to every other area within the network, it is conceivable that such
276 a hierarchical arrangement may not be consistent with defining pathways between every
277 reciprocally connected pair of areas as being FF or FB by comparing the DRs of projections to
278 each other. The absolute value of the difference between DRs of reciprocally connected areal
279 pairs therefore remains an open issue for defining hierarchical distance and designating
280 connections as FF, FB, or lateral[1,2].

281 Cortical Pyr cells typically receive thousands of synaptic contacts, raising the question of
282 how these neurons successfully generate graded spike outputs, without saturating their spike
283 output, in response to varying levels of excitatory input[5]. This problem is compounded by the
284 need for deeper parts of the brain, which are further separated from the outside world than
285 lower areas, to respond robustly and appropriately to sensory input varying in intensity over
286 several orders of magnitude. Pertinently, Pyr cells in higher areas have been shown to have a
287 higher density of dendritic spines than those in lower areas in both primates[4] and rodents[39],
288 indicating that Pyr neurons in higher areas must integrate a larger number of excitatory inputs.
289 To maintain a wide dynamic range over which Pyr cells can signal, inhibitory neurons have been
290 proposed to be critical[5,6]. In particular, PV neurons normalize cortical activity by inhibiting Pyr

291 cells by a level that is proportional to the latter's excitation, thus controlling their gain[16,40,41].
292 Because they are strongly targeted by interareal inputs[11], PV cells are also ideally suited to
293 mediate long-range FFI between areas. Such an interareal inhibitory circuit would make Pyr
294 cells coincidence-detectors[17,42], leading to a reduction of noise levels and the preservation of
295 temporal precision in the target area[43,44]. Coincidence-detection has also been proposed to help
296 achieve a wide dynamic range by allowing only a fraction of excitatory inputs to summate and
297 evoke a spike response[5]. Our observation that L2/3 PV cells are recruited most strongly by
298 pathways transmitting signals from V1 to higher cortical areas imply that signals sent to deeper
299 parts of the brain from more peripheral areas are more potently controlled by inhibition than
300 pathways originating in higher areas. Such a high level of inhibition may be crucial in order for
301 Pyr cells to efficiently integrate excitatory input from a large number of areas. On the other
302 hand, lower I/E levels in FB pathways would broaden the "window of opportunity" for spikes to
303 be integrated and trigger an output in the postsynaptic cell[45], suggesting that FB signals
304 originating in association cortex require less gain control than FF signals. Rather, by broadly
305 modulating the excitability of neurons in lower areas (such as by targeting the primary dendrites
306 of Pyr cells in L1/2), FB pathways are well-placed to prime Pyr cells to selectively respond to FF
307 input in a context-dependent manner[46].

308 Although synaptic inputs to L5 Pyr cells are also denser in higher areas[47], we found that
309 excitation of these neurons in FF and FB pathways is similar and appears to be less strongly
310 counterbalanced by inhibition. This provides a putative mechanism for the previously observed
311 sparse coding in L2/3 Pyr cells and dense excitation in intrinsically burst-spiking L5 Pyr cells,
312 allowing for distinct computational strategies within individual neurons depending on their
313 postsynaptic targets[48-50]. The laminar difference may indicate that, similar to thalamocortical
314 input[51], interareal inputs to L5 are driving Pyr cells. This may enable interareal communication

315 through cortico-thalamo-cortical loops[52] as well as with subcortical motor targets, thereby linking
316 perception and action[53].

317 While PV neurons are a critical component of cortical gain control, it must be noted that
318 they are only one of a number of inhibitory sources[9,10,54]. For instance, neocortical GABAergic
319 interneurons that express vasoactive intestinal polypeptide (VIP) are thought to be an important
320 target of long-range and neuromodulatory inputs[55,56], and in turn, primarily inhibit other
321 interneurons leading to disinhibition of cortical Pyr cells[10,57-59]. Somatostatin (SOM)-expressing
322 interneurons, which include Martinotti cells, make extensive inhibitory contacts with local Pyr
323 cells, and can consequently mediate disynaptic inhibition between neighboring Pyr cells[60,61].
324 SOM neurons have also been shown to provide inhibitory inputs to other interneurons, including
325 PV cells, suggesting a role in the disinhibition of Pyr cells as well[10]. A perhaps surprising source
326 of inhibition and disinhibition is glutamate. By activating pre- and postsynaptic metabotropic
327 receptors in various neocortical circuits, glutamate release can induce suppression of GABA
328 release and inhibition of L4 neurons, respectively[62,63]. Thus, multiple, partially overlapping[54]
329 sources of inhibition may be differentially recruited depending on context, providing a
330 multilayered control of cortical function[57,64].

331 **Materials and methods**

332 All experimental procedures were approved by the Institutional Animal Care and Use Committee
333 at Washington University.

334 ***Animals***

335 For analyzing projection patterns between cortical areas, we used 6 - 8 week-old C57BL/6J
336 male and female mice. In addition, we crossed *Pvalb-Cre* mice (RRID:IMSR_JAX:008069) with
337 Ai9 reporter mice (C57BL/6 background, The Jackson laboratory, Bar Harbor, ME;
338 RRID:IMSR_JAX:007905), which harbored a floxed STOP cassette that prevents transcription

of the fluorescent protein tdTomato (tdT). The crossing resulted in offspring in which PV neurons express tdT. All electrophysiology experiments were performed in male and female PV-tdT mice.

Tracing connections

Mice were anesthetized by intraperitoneal injection of a ketamine/xylazine (86 $mg \cdot kg^{-1}$/13 $mg \cdot kg^{-1}$, IP) mixture and secured in a headholder. Analgesia was achieved by buprenorphine (5 $mg \cdot kg^{-1}$, SC). Callosal connections were labeled by 30-40 pressure injections (20 nl each) of the retrograde tracer bisbenzimide (BB, 5% in H_2O, Sigma) into the right occipital cortex. Interareal projections were labeled by iontophoretic injections (3 μA, 7 s on/off duty cycle for 7 minutes) of the anterograde tracer biotinylated dextran amine (BDA; 10,000 molecular weight, 5% in H_2O; Invitrogen) using a coordinate system whose origin was the intersection between the midline and a perpendicular line drawn from the anterior border of the transverse sinus at the posterior pole of the occipital cortex. The coordinates of the injected areas were (anterior/lateral in mm): V1 (1.1/2.6); LM (1.4/4.1); PM (1.9/1.6). Mice were randomly assigned for injections of a particular area.

Visualization of connections

Three days after the tracer injections, mice were overdosed with ketamine/xylazine, perfused through the heart with heparinized phosphate buffer (PB; 0.1 M, pH 7.4) followed by 4% paraformaldehyde in PB (PFA). Brains were postfixed with 4% PFA and equilibrated in 30% sucrose. To enable areal identification of injection and projection sites, BB labeled callosal landmarks in the left hemisphere were imaged *in situ* under a fluorescence stereomicroscope (Leica MZ16F), equipped with UV optics. The imaged hemispheres were then cut on a freezing microtome at 40 μm in the coronal plane. Sections were collected and numbered as complete series across the full caudo-rostral extent of the hemisphere. Sections were wet mounted onto glass slides and imaged under UV illumination under a fluorescence microscope equipped with

a CCD camera. The sections were then removed from the slides and BDA labeled axonal projections were visualized with avidin and biotinylated HRP (Vectastain ABC Elite) in the presence of H_2O_2 and diaminobenzidine (DAB)[3]. Sections were mounted onto glass slides, coverslipped in DPX and imaged under a microscope equipped with dark field optics.

Virus injections

16 to 23-day-old mice were anesthetized with a mixture of ketamine/xylazine (86 $mg \cdot kg^{-1}$/13 $mg \cdot kg^{-1}$, IP). Held in a stereotaxic apparatus, intracerebral injections of viral vector (AAV2/1.CAG.ChR2-Venus.WPRE.SV40 (Addgene20071); Vector Core, University of Pennsylvania)[23] were made with glass pipettes (tip diameter 25 μm) connected to a Nanoject II Injector (Drummond). Injections were performed stereotaxically into V1, LM or PM, 0.3 and 0.5 mm below the pial surface, to ensure infection of neurons throughout the thickness of cortex. The total volume of the viral vector at each depth was 46 nl. Successful injections resulted in the simultaneous expression of Channelrhodopsin-2 (ChR2) and the fluorescent protein Venus in terminals of outgoing axons. Mice were randomly selected for the study of a particular pathway.

Slice electrophysiology

30 to 45 day-old mice, 14-21 days after viral injection, were anesthetized with a mixture of ketamine/xylazine (86 $mg \cdot kg^{-1}$/13 $mg \cdot kg^{-1}$, IP), and transcardially perfused with 10 ml of ice-cold oxygenated 95% O_2/5% CO_2 dissection solution (sucrose-ACSF) containing (in mM): 228 sucrose, 2.5 KCl, 1.25 NaH_2PO_4, 25 $NaHCO_3$, 0.5 $CaCl_2$, 7.0 $MgCl_2$, and 10 D-glucose. Mice were decapitated, the brain removed from the skull, and mounted on the specimen plate of Leica Vibratome (Leica VT1200) with a cyanoacrylate adhesive (Krazy Glue). Visual cortex was cut coronally at 350 μm in ice-cold sucrose-ACSF. Slices were transferred to a holding chamber filled with ACSF containing (in mM): 125 $NaCl_2$, 2.5 KCl, 1.25 NaH_2PO_4, 25 $NaHCO_3$, 2.0 $CaCl_2$, 1.0 $MgCl_2$, and 25 D-glucose. Slices were incubated in ACSF for 30 minutes at 34°C and maintained at room temperature until recordings. Acute slices were superfused with

recirculating oxygenated ACSF at room temperature in a submersion chamber mounted on the fixed stage of an upright microscope (Nikon Eclipse FN1). For subcellular, optogenetic mapping experiments, 1 μM TTX and 100 μM 4-AP were added to the bath in order to block action potentials (and therefore polysynaptic excitation) and fast repolarizing potassium currents. Whole-cell patch clamp recordings were performed with borosilicate pipettes (4-6 MΩ resistance). The pipette solution contained (in mM) 128 potassium gluconate, 4 $MgCl_2$, 10 HEPES, 1 EGTA, 4 Na_2ATP, 0.4 Na_2GTP, 10 sodium phosphocreatine, 3 sodium L-ascorbate, and 3 mg/ml biocytin. The pH was adjusted to 7.2-7.3, and osmolarity to 290 mOsm. Fluorescence of ChR2/Venus-expressing fibers and tdT-expressing PV neurons was imaged with a CCD camera (Retiga 2000DC, QImaging). Pyr and PV neurons lying within maximal levels of ChR2/Venus-expressing axonal projections were selected for recordings. PV neurons were identified by tdT expression. For sCRACM experiments (see below), neurons were voltage clamped at -70 mV. All voltage-clamp and current-clamp experiments were performed using the Ephus software[65] (Vidrio Technologies), an Axopatch 700B amplifier (Molecular devices), and a data acquisition (DAQ) device (NI USB-6259, National Instruments Corp., Austin, TX).

Optogenetic photostimulation

Photostimulation of ChR2-expressing fibers was achieved by a blue laser (473 nm; CrystaLaser) delivered in an 8×16 grid in which stimulation points were spaced 75 μm apart, one spot at a time, 400 ms between laser delivery at each spot. The grid was aligned such that the longer axis was perpendicular to the pial surface and stimulated spots in all six layers. The position of the laser beam was controlled by galvanometer scanners (Cambridge Scanning), and the duration of stimulation (1 ms) was controlled by a shutter (LS6, Uniblitz). The laser beam (~20 μm at half maximal intensity) passed through a Pockels cell (ConOptics) and an air objective (4x PlanApo). Because the expression level of ChR2-Venus in interareal axons varied across slices and animals, the laser power was adjusted in every slice so that the largest

414 $EPSC_{sCRACM}$ (EPSC recorded under sCRACM conditions) in a neuron did not increase upon
415 increasing laser intensity. Importantly, the laser power was constant for all recordings made in
416 the same slice, in order to compare $EPSCs_{sCRACM}$ between neighboring neurons. The laser
417 power measured at the image plane was 0.7 - 1 mW/cm^2. Photostimulation was repeated three
418 to five times for each neuron. The shutter timing and the position of galvanometer mirrors was
419 controlled by Ephus[65].

420 ***Immunostaining***

421 After recordings, slices were fixed in 4% PFA, cryoprotected in 30% sucrose and re-sectioned
422 on a freezing microtome at 40 µm. The sections were then incubated with an antibody against
423 the type 2 muscarinic acetylcholine receptor (M2; 1:500 in PB; MAB367, Millipore;
424 RRID:AB_94952) and stained with Alexa Fluor 647-labeled IgG (1:500 in 10% NGS; A21247;
425 Invitrogen). M2-expression was imaged under a microscope equipped with IR fluorescence
426 optics. The intense M2-expression in V1 was used as landmark for assigning Venus labeled
427 axonal projections to LM and PM [24].

428 ***Dendritic morphology***

429 M2 stained sections containing biocytin-filled neurons were treated with 1% H_2O_2, and
430 incubated in avidin and biotinylated horseradish peroxidase (Vectastain ABC Elite) in the
431 presence of DAB. The soma and dendritic arbor of biocytin-filled neurons were reconstructed
432 under a 60x oil objective using Neurolucida (MBF Bioscience; RRID:SCR_001775).

433 ***Data analysis and statistics***

434 *Areal hierarchy analysis*

435 One BDA injection was performed in each mouse, and injection into a particular area (V1, LM,
436 or PM) was performed in two mice (n = 6 animals for all injections). Three adjacent sections
437 containing projections in the target area were typically used for analyses of each pathway in
438 each brain. Projections were assigned to areas by their location relative to retrogradely

bisbenzimide-labeled callosal landmarks[20] and by their relative positions to each other. Callosal landmarks were imaged *in situ* before sectioning the brain. Sections were numbered from the posterior pole of cortex so that the callosal landmarks seen in the coronal plane could be matched to specific locations (multiplying section number by section thickness) of the *in situ* pattern. BDA labeled injection sites and axonal projections were then superimposed onto the callosal pattern observed in the same section, and terminations were assigned to specific areas according to the map by Wang and Burkhalter [20].

Grayscale images of anterogradely BDA-labeled axonal projections in target areas were used for analyses of termination patterns. The coronal sections were imaged under 8x magnification. A custom-written MATLAB script were used to generate contour plots of the optical density of axons after processing the image through a circular averaging 2-D filter. Previous analyses have shown that optical density correlates with bouton density[24]. Regions within contours of the highest 70% of optical densities in L2-4 and in L1 were used to generate the L2-4:L1 ratio for each slice. The optical density was measured using the mean *Gray Value* in ImageJ (RRID:SCR_003070) within the 70% contour.

Electrophysiology analyses

EPSCs recorded upon photostimulation, > 4 times the standard deviation of baseline, were used for analysis. Individual pixel values for each position of the 8×16 photostimulus grid was calculated as the average EPSC value within 75 ms after photostimulation, and expressed in pA. These calculations were done by custom-written MATLAB scripts. EPSCs at each location of the grid were averaged over three to five repetitions of photostimulation to generate sCRACM maps for each neuron. To compare the total interareal input to pairs of PV and Pyr neurons in the target area, we summed the pixel values for each cell, and compared the total EPSC value of PV and Pyr neurons lying within ~100 µm of each other, either in L2/3 or in L5. For comparison of mean EPSCs per stimulation point (Figure 3 – figure supplement 1), we

averaged pixel values with significant responses (> 4 times standard deviation of baseline) for each cell. For statistical analysis of differences of interareal input to PV and Pyr cells for a particular pathway, we generated scatter plots (for example, Figure 2f) in which each data point plotted the total $EPSC_{sCRACM}$ from a PV neuron (vertical axis) against the total $EPSC_{sCRACM}$ from its Pyr neighbor (horizontal axis). The solid black line in such a scatter plot was generated by connecting the origin (0, 0) to the geometric mean of all $EPSC_{PV}/EPSC_{Pyr}$ ratios for the respective pathway. The solid blue line was plotted in a similar fashion, but after normalization to the average cell conductance. The non-parametric Wilcoxon signed-rank test was used for comparing total EPSCs between cell types within pairs. For average heat maps of multiple PV or Pyr neurons, we used a smoothening function in MATLAB that interpolates EPSC values between pixels.

All box plots show mean (black squares), median (horizontal line within box), 25-75 percentile range (horizontal lines bounding box) and outermost points within upper and lower inner fences (whiskers). The non-parametric Kruskal-Wallis test was used to compare mean $EPSC_{PV}/EPSC_{Pyr}$ ratios between pathways, while the One-Way Analysis of Variance (ANOVA) was used for comparing means of groups whose probability distributions were expected to be parametric. Statistical significance was $p < 0.05$. No statistical method was used to predetermine number of neurons, slices, or animals used (sample size), but our sample sizes were consistent with other comparable experiments[3,15,27].

References

1 Felleman, D. J. & Van Essen, D. C. Distributed hierarchical processing in the primate cerebral cortex. *Cerebral Cortex* **1**, 1-47 (1991).

2 Coogan, T. A. & Burkhalter, A. Hierarchical organization of areas in rat visual cortex. *The Journal of Neuroscience : the official journal of the Society for Neuroscience* **13**, 3749-3772 (1993).

3 Wang, Q., Sporns, O. & Burkhalter, A. Network analysis of corticocortical connections reveals ventral and dorsal processing streams in mouse visual cortex. *The Journal of Neuroscience : the official journal of the Society for Neuroscience* **32**, 4386-4399, doi:10.1523/JNEUROSCI.6063-11.2012 (2012).

4 Elston, G. N. Cortex, cognition and the cell: new insights into the pyramidal neuron and prefrontal function. *Cerebral Cortex* **13**, 1124-1138 (2003).

5 Shadlen, M. N. & Newsome, W. T. The variable discharge of cortical neurons: implications for connectivity, computation, and information coding. *The Journal of Neuroscience : the official journal of the Society for Neuroscience* **18**, 3870-3896 (1998).

6 Pouille, F., Marin-Burgin, A., Adesnik, H., Atallah, B. V. & Scanziani, M. Input normalization by global feedforward inhibition expands cortical dynamic range. *Nature Neuroscience* **12**, 1577-1585, doi:10.1038/nn.2441 (2009).

7 Johnson, R. R. & Burkhalter, A. Microcircuitry of forward and feedback connections within rat visual cortex. *The Journal of Comparative Neurology* **368**, 383-398, doi:10.1002/(SICI)1096-9861(19960506)368:3<383::AID-CNE5>3.0.CO;2-1 (1996).

8 Yoshimura, Y. & Callaway, E. M. Fine-scale specificity of cortical networks depends on inhibitory cell type and connectivity. *Nature Neuroscience* **8**, 1552-1559, doi:10.1038/nn1565 (2005).

9 Jiang, X. *et al.* Principles of connectivity among morphologically defined cell types in adult neocortex. *Science* **350**, aac9462, doi:10.1126/science.aac9462 (2015).

10 Pfeffer, C. K., Xue, M., He, M., Huang, Z. J. & Scanziani, M. Inhibition of inhibition in visual cortex: the logic of connections between molecularly distinct interneurons. *Nature neuroscience* **16**, 1068-1076, doi:10.1038/nn.3446 (2013).

11 Gonchar, Y. & Burkhalter, A. Differential subcellular localization of forward and feedback interareal inputs to parvalbumin expressing GABAergic neurons in rat visual cortex. *The Journal of Comparative Neurology* **406**, 346-360 (1999).

12 Gonchar, Y. & Burkhalter, A. Distinct GABAergic targets of feedforward and feedback connections between lower and higher areas of rat visual cortex. *The Journal of Neuroscience : the official journal of the Society for Neuroscience* **23**, 10904-10912 (2003).

13 Hangya, B., Pi, H. J., Kvitsiani, D., Ranade, S. P. & Kepecs, A. From circuit motifs to computations: mapping the behavioral repertoire of cortical interneurons. *Current Opinion in Neurobiology* **26**, 117-124, doi:10.1016/j.conb.2014.01.007 (2014).

14 Dong, H., Shao, Z., Nerbonne, J. M. & Burkhalter, A. Differential depression of inhibitory synaptic responses in feedforward and feedback circuits between different areas of mouse visual cortex. *The Journal of Comparative Neurology* **475**, 361-373, doi:10.1002/cne.20164 (2004).

15 Yang, W., Carrasquillo, Y., Hooks, B. M., Nerbonne, J. M. & Burkhalter, A. Distinct balance of excitation and inhibition in an interareal feedforward and feedback circuit of mouse visual cortex. *The Journal of Neuroscience : the official journal of the Society for Neuroscience* **33**, 17373-17384, doi:10.1523/JNEUROSCI.2515-13.2013 (2013).

16 Atallah, B. V., Bruns, W., Carandini, M. & Scanziani, M. Parvalbumin-expressing interneurons linearly transform cortical responses to visual stimuli. *Neuron* **73**, 159-170, doi:10.1016/j.neuron.2011.12.013 (2012).
17 Gabernet, L., Jadhav, S. P., Feldman, D. E., Carandini, M. & Scanziani, M. Somatosensory integration controlled by dynamic thalamocortical feed-forward inhibition. *Neuron* **48**, 315-327, doi:10.1016/j.neuron.2005.09.022 (2005).
18 Cardin, J. A., Kumbhani, R. D., Contreras, D. & Palmer, L. A. Cellular mechanisms of temporal sensitivity in visual cortex neurons. *The Journal of Neuroscience : the official journal of the Society for Neuroscience* **30**, 3652-3662, doi:10.1523/JNEUROSCI.5279-09.2010 (2010).
19 Okun, M. & Lampl, I. Instantaneous correlation of excitation and inhibition during ongoing and sensory-evoked activities. *Nature Neuroscience* **11**, 535-537, doi:10.1038/nn.2105 (2008).
20 Wang, Q. & Burkhalter, A. Area map of mouse visual cortex. *The Journal of Comparative Neurology* **502**, 339-357, doi:10.1002/cne.21286 (2007).
21 Rockland, K. S. & Virga, A. Terminal arbors of individual "feedback" axons projecting from area V2 to V1 in the macaque monkey: a study using immunohistochemistry of anterogradely transported Phaseolus vulgaris-leucoagglutinin. *The Journal of Comparative Neurology* **285**, 54-72, doi:10.1002/cne.902850106 (1989).
22 Henry, G. H., Salin, P. A. & Bullier, J. Projections from Areas 18 and 19 to Cat Striate Cortex: Divergence and Laminar Specificity. *The European Journal of Neuroscience* **3**, 186-200 (1991).
23 Petreanu, L., Mao, T., Sternson, S. M. & Svoboda, K. The subcellular organization of neocortical excitatory connections. *Nature* **457**, 1142-1145, doi:10.1038/nature07709 (2009).
24 Wang, Q., Gao, E. & Burkhalter, A. Gateways of ventral and dorsal streams in mouse visual cortex. *The Journal of Neuroscience : the official journal of the Society for Neuroscience* **31**, 1905-1918, doi:10.1523/JNEUROSCI.3488-10.2011 (2011).
25 Ji, W. *et al.* Modularity in the Organization of Mouse Primary Visual Cortex. *Neuron* **87**, 632-643, doi:10.1016/j.neuron.2015.07.004 (2015).
26 Packer, A. M. & Yuste, R. Dense, unspecific connectivity of neocortical parvalbumin-positive interneurons: a canonical microcircuit for inhibition? *The Journal of Neuroscience : the official journal of the Society for Neuroscience* **31**, 13260-13271, doi:10.1523/JNEUROSCI.3131-11.2011 (2011).
27 Mao, T. *et al.* Long-range neuronal circuits underlying the interaction between sensory and motor cortex. *Neuron* **72**, 111-123, doi:10.1016/j.neuron.2011.07.029 (2011).
28 Hull, C., Isaacson, J. S. & Scanziani, M. Postsynaptic mechanisms govern the differential excitation of cortical neurons by thalamic inputs. *The Journal of Neuroscience : the official journal of the Society for Neuroscience* **29**, 9127-9136, doi:10.1523/JNEUROSCI.5971-08.2009 (2009).
29 Povysheva, N. V. *et al.* Properties of excitatory synaptic responses in fast-spiking interneurons and pyramidal cells from monkey and rat prefrontal cortex. *Cerebral Cortex* **16**, 541-552, doi:10.1093/cercor/bhj002 (2006).
30 Marshel, J. H., Garrett, M. E., Nauhaus, I. & Callaway, E. M. Functional specialization of seven mouse visual cortical areas. *Neuron* **72**, 1040-1054, doi:10.1016/j.neuron.2011.12.004 (2011).
31 Andermann, M. L., Kerlin, A. M., Roumis, D. K., Glickfeld, L. L. & Reid, R. C. Functional specialization of mouse higher visual cortical areas. *Neuron* **72**, 1025-1039, doi:10.1016/j.neuron.2011.11.013 (2011).
32 Roth, M. M., Helmchen, F. & Kampa, B. M. Distinct functional properties of primary and posteromedial visual area of mouse neocortex. *The Journal of Neuroscience : the official*

journal of the Society for Neuroscience **32**, 9716-9726, doi:10.1523/JNEUROSCI.0110-12.2012 (2012).
33 Glickfeld, L. L., Reid, R. C. & Andermann, M. L. A mouse model of higher visual cortical function. *Current Opinion in Neurobiology* **24**, 28-33, doi:10.1016/j.conb.2013.08.009 (2014).
34 Cardin, J. A. *et al.* Driving fast-spiking cells induces gamma rhythm and controls sensory responses. *Nature* **459**, 663-667, doi:10.1038/nature08002 (2009).
35 Bastos, A. M. *et al.* Visual areas exert feedforward and feedback influences through distinct frequency channels. *Neuron* **85**, 390-401, doi:10.1016/j.neuron.2014.12.018 (2015).
36 Price, D. J. & Zumbroich, T. J. Postnatal development of corticocortical efferents from area 17 in the cat's visual cortex. *The Journal of Neuroscience : the official journal of the Society for Neuroscience* **9**, 600-613 (1989).
37 Coogan, T. A. & Burkhalter, A. Conserved patterns of cortico-cortical connections define areal hierarchy in rat visual cortex. *Experimental Brain Research* **80**, 49-53 (1990).
38 Cauller, L. Layer I of primary sensory neocortex: where top-down converges upon bottom-up. *Behavioural Brain Research* **71**, 163-170 (1995).
39 Elston, G. N. *et al.* Specialization of pyramidal cell structure in the visual areas V1, V2 and V3 of the South American rodent, Dasyprocta primnolopha. *Brain Research* **1106**, 99-110, doi:10.1016/j.brainres.2006.05.100 (2006).
40 Wilson, N. R., Runyan, C. A., Wang, F. L. & Sur, M. Division and subtraction by distinct cortical inhibitory networks in vivo. *Nature* **488**, 343-348, doi:10.1038/nature11347 (2012).
41 Xue, M., Atallah, B. V. & Scanziani, M. Equalizing excitation-inhibition ratios across visual cortical neurons. *Nature* **511**, 596-600, doi:10.1038/nature13321 (2014).
42 Pouille, F. & Scanziani, M. Enforcement of temporal fidelity in pyramidal cells by somatic feed-forward inhibition. *Science* **293**, 1159-1163, doi:10.1126/science.1060342 (2001).
43 Bruno, R. M. Synchrony in sensation. *Current Opinion in Neurobiology* **21**, 701-708, doi:10.1016/j.conb.2011.06.003 (2011).
44 Zhu, Y., Qiao, W., Liu, K., Zhong, H. & Yao, H. Control of response reliability by parvalbumin-expressing interneurons in visual cortex. *Nature Communications* **6**, 6802, doi:10.1038/ncomms7802 (2015).
45 Isaacson, J. S. & Scanziani, M. How inhibition shapes cortical activity. *Neuron* **72**, 231-243, doi:10.1016/j.neuron.2011.09.027 (2011).
46 Larkum, M. A cellular mechanism for cortical associations: an organizing principle for the cerebral cortex. *Trends in Neurosciences* **36**, 141-151, doi:10.1016/j.tins.2012.11.006 (2013).
47 Elston, G. N. & Rosa, M. G. Pyramidal cells, patches, and cortical columns: a comparative study of infragranular neurons in TEO, TE, and the superior temporal polysensory area of the macaque monkey. *The Journal of neuroscience : the official journal of the Society for Neuroscience* **20**, RC117 (2000).
48 Harris, K. D. & Mrsic-Flogel, T. D. Cortical connectivity and sensory coding. *Nature* **503**, 51-58, doi:10.1038/nature12654 (2013).
49 Hefti, B. J. & Smith, P. H. Anatomy, physiology, and synaptic responses of rat layer V auditory cortical cells and effects of intracellular GABA(A) blockade. *Journal of Neurophysiology* **83**, 2626-2638 (2000).
50 Schubert, D., Kotter, R. & Staiger, J. F. Mapping functional connectivity in barrel-related columns reveals layer- and cell type-specific microcircuits. *Brain Structure & Function* **212**, 107-119, doi:10.1007/s00429-007-0147-z (2007).
51 Constantinople, C. M. & Bruno, R. M. Deep cortical layers are activated directly by thalamus. *Science* **340**, 1591-1594, doi:10.1126/science.1236425 (2013).

52 Guillery, R. W. & Sherman, S. M. Thalamic relay functions and their role in corticocortical communication: generalizations from the visual system. *Neuron* **33**, 163-175 (2002).
53 Kim, E. J., Juavinett, A. L., Kyubwa, E. M., Jacobs, M. W. & Callaway, E. M. Three Types of Cortical Layer 5 Neurons That Differ in Brain-wide Connectivity and Function. *Neuron* **88**, 1253-1267, doi:10.1016/j.neuron.2015.11.002 (2015).
54 Gonchar, Y., Wang, Q. & Burkhalter, A. Multiple distinct subtypes of GABAergic neurons in mouse visual cortex identified by triple immunostaining. *Frontiers in Neuroanatomy* **1**, 3, doi:10.3389/neuro.05.003.2007 (2007).
55 Fu, Y. *et al.* A cortical circuit for gain control by behavioral state. *Cell* **156**, 1139-1152, doi:10.1016/j.cell.2014.01.050 (2014).
56 Reimer, J. *et al.* Pupil fluctuations track fast switching of cortical states during quiet wakefulness. *Neuron* **84**, 355-362, doi:10.1016/j.neuron.2014.09.033 (2014).
57 Kepecs, A. & Fishell, G. Interneuron cell types are fit to function. *Nature* **505**, 318-326, doi:10.1038/nature12983 (2014).
58 Pi, H. J. *et al.* Cortical interneurons that specialize in disinhibitory control. *Nature* **503**, 521-524, doi:10.1038/nature12676 (2013).
59 Karnani, M. M. *et al.* Opening Holes in the Blanket of Inhibition: Localized Lateral Disinhibition by VIP Interneurons. *The Journal of Neuroscience : the official journal of the Society for Neuroscience* **36**, 3471-3480, doi:10.1523/JNEUROSCI.3646-15.2016 (2016).
60 Fino, E. & Yuste, R. Dense inhibitory connectivity in neocortex. *Neuron* **69**, 1188-1203, doi:10.1016/j.neuron.2011.02.025 (2011).
61 Silberberg, G. & Markram, H. Disynaptic inhibition between neocortical pyramidal cells mediated by Martinotti cells. *Neuron* **53**, 735-746, doi:10.1016/j.neuron.2007.02.012 (2007).
62 Liu, T., Petrof, I. & Sherman, S. M. Modulatory effects of activation of metabotropic glutamate receptors on GABAergic circuits in the mouse cortex. *Journal of Neurophysiology* **111**, 2287-2297, doi:10.1152/jn.00730.2013 (2014).
63 Lee, C. C. & Sherman, S. M. Glutamatergic inhibition in sensory neocortex. *Cerebral Cortex* **19**, 2281-2289, doi:10.1093/cercor/bhn246 (2009).
64 Pakan, J. M. *et al.* Behavioral-state modulation of inhibition is context-dependent and cell type specific in mouse visual cortex. *eLife* **5**, doi:10.7554/eLife.14985 (2016).
65 Suter, B. A. *et al.* Ephus: multipurpose data acquisition software for neuroscience experiments. *Frontiers in Neural Circuits* **4**, 100, doi:10.3389/fncir.2010.00100 (2010).

Acknowledgements

We thank Katia Valkova and Weiguo Yang for technical assistance. Work supported by R01 EY016184, R01 EY022090, and the McDonnell Center for Systems Neuroscience.

Author contributions

A.B. and R.D.D. conceptualized and designed experiments. Q.W. and A.B. performed BDA tracing experiments. R.D.D. performed optogenetic and electrophysiological experiments. R.D.D. and A.M.M. analyzed data. P.B. assisted in pilot paired recordings experiments. A.B. and R.D.D. wrote the paper.

Competing financial interests

The authors declare no competing financial interests.

Figure titles and legends

Figure 1. Hierarchy between V1, LM, and PM. (**a**) Rostrocaudal series of coronal slices through left hemisphere showing anterogradely labelled axonal projections (yellow/orange) after V1 was injected with BDA. Retrogradely labelled callosally projecting neurons (light cyan), upon injection of bisbenzimide in the right hemisphere, act as landmarks for identification of areas [20]. Numbers denote sections corresponding to positions shown in inset. See Figure 1 – figure supplement 1 for higher magnification of areas within dotted squares. Projection to LM adjacent to LI in section 33 is indicated. Arrowhead indicates region in V1 near injected site. *Inset*: *In situ* image of retrograde bisbenzimide-labelled callosally projecting neurons in the left hemisphere. Injection site in V1 (asterisk) and positions of coronal slices shown above are indicated. Scale bars, 1 mm. (**b**) Optical density of axonal projections in the target areas of the indicated pathways, normalized to peak density. Contours connect regions with similar optical densities. Arrowheads denote edge of slice and edge artifacts due to interpolation of optical density with dark background. (**c**) Color-coded heat map of L2-4:L1 density ratio (DR) for each of 25 distinct cortico-cortical connections. Blocks in grey indicate projections that were too weak to analyze. V1 exhibits the highest DRs, and PM the lowest, indicating the relative hierarchical positions of the areas. (**d**) The mean DR for all target areas is highest for V1, intermediate for LM, and lowest for PM; ***$p < 0.001$, Mann-Whitney U-test. (**e**) Our schematic interpretation of the hierarchy of V1, LM, and PM in visual processing. Feedforward pathways are denoted in green, feedback in red.

Figure 1 – figure supplement 1. Darkfield images of the termination patterns of BDA-labelled axonal projections from V1 to LM, LI, P, POR, AL, PM, RL, AM and A. Images are taken from the boxed regions shown in ***1A***. All projections are FF, which target L2-4 more strongly than L1. Scale bar, 0.5 mm.

Figure 1 – figure supplement 2. Coronal sections showing anterogradely labelled axons (yellow/orange) from LM to V1, LI, P, POR, AL, PM, RL, AM and A, upon BDA injection into LM. Calossally projecting neurons (light cyan) are labelled retrogradely after injection of bisbenzimide into the opposite hemisphere. Boxed regions show projections to each of the nine target areas. Asterisk in coronal section 28 denotes injection site in LM. Scale bar, 1 mm. *Inset*: *In situ* image of left hemisphere shows retrogradely bizbenzimide-labelled neurons marking callosal landmarks. Injection site in LM (asterisk) and numbers of coronal slices shown above are indicated. Scale bar, 1 mm.

Figure 1 – figure supplement 3. Axonal projections (yellow/orange) from PM to V1, LM, LI, P, POR, AL, RL, AM and A, upon BDA injection into PM. Calossally projecting neurons (light blue, labeled with bisbenzimide) provide landmarks for areal identification[20]. Boxed regions show projections to target areas. Asterisk in section 48 denotes region in PM adjacent to injection site. *Inset*: Left hemisphere *in situ* shows injection site in PM (asterisk) and positions of coronal slices shown above. Scale bars, 1 mm.

Figure 2. Subcellular ChR2-assisted mapping of V1→PM connections to L2/3 PV and Pyr cells. (**a**) Coronal slices showing injection (left) and target (right) sites two weeks after the injection of AAV2/1.CAG.ChR2-Venus.WPRE.SV40 into V1. Scale bar, 500 µm. Select target areas indicated in right panel. SC, superior colliculus. (**b**) Schematic of laser-scanning photostimulation of ChR2-expressing axon terminals during whole-cell recording of a biocytin-filled neuron. TTX and 4-AP are added to the bath solution, and the blue laser is delivered successively one spot at a time in a grid pattern separated by 75 µm. (**c**) $EPSCs_{sCRACM}$ in a PV (left) and a neighboring Pyr (right) cell upon photostimulation. Grey shapes denote location of cell body of recorded neuron. (**d**) Heat map of mean EPSCs within 75 µs after photostimulation for the EPSCs in ***3c***. Reconstructions of respective biocytin-filled neurons are superimposed on heat map. (**e**) Average heat map of 14 neighboring PV-Pyr cell pairs in L2/3 receiving V1→PM input, normalized to largest pixel value between a pair. PV cells receive substantially stronger input. (**f**) Scatter plot denoting the relative input strengths to 14 PV-Pyr cell pairs. Each data point represents a pair with the respective EPSCs in the PV (vertical axis) and the Pyr (horizontal axis) cell. The total EPSC in PV cells is significantly larger than that in neighboring Pyr cells ($p < 0.001$, Wilcoxon signed-rank test). Solid black line: mean slope, blue line: mean slope after normalizing currents to mean cell conductance. (**g**) The mean time to peak of EPSCs after photostimulation is larger in Pyr cells than in PV cells (*$p < 0.05$, paired t-test).

Figure 2 – figure supplement 1. V1→PM pathway in a PV-tdT mouse. (**a-e**) Image of coronal section two weeks after the injection of AAV2/1.CAG.ChR2-Venus.WPRE.SV40 into V1. Slice includes areas PM, AL, and V1. PV cells in red (***a,c***), ChR2-Venus-expressing axons in green (***b,c***). Merged image in (***c***). Dotted lines demarcate AL/V1 and V1/PM boundaries indicated by the sharp decline of M2 expression between V1 and surrounding areas (***d***). V1 is characterized by a thick band of M2 expression (purple) in L4, showing that the axonal terminations (green) lie outside V1 (***d,e***). (**f**) Higher magnification view of PM from (***c***) with layers indicated.

Figure 2 – figure supplement 2. Paired recordings of excitation-dependent, PV cell-mediated inhibition of Pyr cells. (**a**) Coronal section through V1 and PM of a *PV-Cre* × Ai9 mouse in which PV cells express tdT (red). Scale bar, 200 µm. *Inset*: Higher magnification of boxed region shows a high density of tdT-expressing dendrites in L1 even though PV cell bodies are not found in this layer. (**b**) *Left*, PV cell identified by tdT expression targeted for whole-cell recordings. Scale bar, 20 µm. *Middle*, same cell as in left panel, imaged under DIC-IR optics. PV cell shows a non-adapting, fast-spiking firing pattern (*inset*, red trace) upon current injection. *Right*, A Pyr cell under infrared optics exhibits an adapting spiking physiology (blue trace) upon current injection. (**c**) Schematic of paired recordings of a PV (red) and a Pyr (blue) cell. Successively increasing current steps (100, 200, 300 and 400 pA) were injected into the PV cell under current clamp, and inhibitory currents (IPSCs) were recorded in the Pyr cell held at 0 mV under voltage clamp. (**d**) Example trace in a L2/3 PV-Pyr connected pair in PM. Increasing current injections into the PV cell results in stronger inhibitory drive to the Pyr cell. (**e**) Example traces of a connected PV-Pyr cell pair in L5 of PM. (**f**) Pooled data from connected PV-Pyr pairs in L2/3 (left) and L5 (right) show that increasing the excitation of PV cells results in stronger inhibition of synaptically connected Pyr cells ($p < 0.001$ for both sets of data; ANOVA). Mean IPSCs measured over 75 ms after start of current step. (**g**) Probability of a PV cell connected to a neighboring Pyr cell (< 100 µm) in L2/3 and L5 of PM.

Figure 3. Lower I/E balance in PM→V1 pathway. (**a**) Coronal slices showing AAV2/1.CAG.ChR2-Venus (green) injection in PM (top) and axonal labelling in target areas (bottom) of a PV-tdT (red) mouse. Scale bar, 1 mm. (**b**) $EPSCs_{sCRACM}$ in a pair of neighboring PV (left) and Pyr cells (right) in V1. (**c**) Heat map of the currents in ***4b*** superimposed with biocytin-filled neurons (white). Note significant input into L1 of both cell types. (**d**) PV cells, on average, exhibit larger $EPSCs_{sCRACM}$ than neighboring Pyr cells in the PM→V1 pathway ($p < 0.02$, Wilcoxon signed-rank test). Solid black line: mean slope of data points; blue line: mean slope after normalization to cell conductance. (**e**) Normalized, mean heat map of all L2/3 pairs in the $FB_{PM→V1}$ pathway. (**f**) EPSCs are faster in L2/3 PV than in neighboring Pyr cells upon stimulation of $FB_{PM→V1}$ axon terminals (*$p < 0.001$, paired t-test). (**g**) The interareal excitation of PV cells, normalized to that of neighboring Pyr cells, is on average larger in the $FF_{V1→PM}$ than in the $FB_{PM→V1}$ pathway (***$p < 0.001$, Mann-Whitney U-test). (**h**) Total currents in each row of the 8×16 grid for $FF_{V1→PM}$ and $FB_{PM→V1}$ pathways plotted against relative position of each of the 16 rows. EPSCs normalized to total EPSC in each cell-type. pia, pia mater; wm, white matter. (**i**) Interareal input to L1 is stronger in the $FB_{PM→V1}$ than in the $FF_{V1→PM}$ pathway in both cell types (**$p < 0.01$, ***$p < 0.001$, Mann-Whitney U-test). L1 input was calculated as the mean of the total input to each row of the 8×16 grid that resided in L1, presented as the percentage of the total input to the neuron.

Figure 3 – figure supplement 1. (**a**) The EPSC per 75 µm x 75 µm pixel, calculated as $pA/µm^2$, is larger in PV than in Pyr cells in $FF_{V1→PM}$. (**b**) Individual PV cells receive interareal $FF_{V1→PM}$ input over a larger area than Pyr cells (***$p < 0.001$). (**c**) The EPSC per pixel in PV and Pyr cells is not significantly different in the $FB_{PM→V1}$ pathway. (**d**) PV cells receive input over a larger area than Pyr cells in the $FB_{PM→V1}$ pathway (*$p < 0.05$).

Figure 4. Interareal recruitment of L2/3 PV cells depends on pathway and hierarchical distance between areas. (**a**) $EPSCs_{sCRACM}$ in a L2/3 PV (left) and Pyr (right) cell in the $FF_{LM→PM}$ pathway. (**b**) sCRACM map of EPSCs in ***5a*** with reconstructed neuron positions. (**c**) Scatter plot of all PV-Pyr cell pairs in the L2/3 $FF_{LM→PM}$ pathway. PV cells exhibit larger currents than Pyr cells. (**d-f**) Similar data as in (***a-c***) but for the L2/3 $FB_{PM→LM}$ pathway. Note stronger L1 input in this pathway. (**g**) PV cell excitation, normalized to that of a neighboring Pyr cell, is stronger in the $FF_{V1→PM}$ than in the hierarchically shorter $FF_{LM→PM}$ pathway (*$p < 0.05$, Mann-Whiteney U-test). (**h**) Normalized PV cell excitation is stronger in the $FB_{PM→LM}$ than in the hierarchically longer $FB_{PM→V1}$ pathway (*$p < 0.05$, Mann-Whiteney U-test). (**i**) Normalized plot of total current in each row of the 8×16 grid, plotted against row position. EPSCs normalized to total current in each cell-type. (**j**) The total $EPSCs_{sCRACM}$ in a PV cell, normalized to the total $EPSCs_{sCRACM}$ in a neighboring Pyr cell, depends on directionality of the pathway and hierarchical distance between areas. Red boxes represent data describing connections between V1 and LM from Yang et al, 2013. ***$p < 0.001$, Kruskal-Wallis test.

Figure 4 – figure supplement 1. (**a**) Normalized heat maps of average EPSCs in L2/3 PV cells in the $FF_{LM→PM}$ and $FB_{PM→LM}$ pathways. EPSC values normalized to peak pixel in each panel. (**b**) Interareal input to L1 is stronger for PV cells in the $FB_{PM→LM}$ pathway than in $FF_{LM→PM}$. L1 input calculated as average input to each row of the 8×16 grid that resided in L1, normalized to total EPSC recorded from the cell. (**c**) Normalized heat maps of average EPSCs in L2/3 Pyr cells in $FF_{LM→PM}$ and $FB_{PM→LM}$. EPSC values normalized to peak value within panel. (**d**) Interareal input to L1 is stronger for Pyr cells in the $FB_{PM→LM}$ than in the $FF_{LM→PM}$ pathway.

Figure 4 – figure supplement 2. (**a**) Total EPSC per row plotted against row position for L2/3 PV and Pyr cells in the $FF_{V1\rightarrow PM}$, $FF_{LM\rightarrow PM}$, $FB_{PM\rightarrow LM}$ and $FB_{PM\rightarrow V1}$ pathways. Strongest EPSCs in both cell types are observed in the LM→PM pathway, with weak EPSCs to Pyr cells in the $FF_{V1\rightarrow PM}$ pathway. (**b**) $FF_{LM\rightarrow PM}$ inputs result in the strongest current density (measured as EPSC/pixel, converted to $pA/\mu m^2$) among all examined L2/3 pathways for both PV and Pyr cells (#$p < 0.05$ against each of the other three pathways) (**c**) The total area over which individual PV cells receive input is not significantly different for PV cells. Pyr cells in the $FF_{V1\rightarrow PM}$ pathway receive input over the smallest area (#$p < 0.05$ against each of the other pathways). (**d**) The mean time to peak for interareal EPSCs is smaller in PV than in Pyr cells in both $FF_{LM\rightarrow PM}$ and $FB_{PM\rightarrow LM}$ pathways.

Figure 5. FF input to L5 neurons. (**a**) $FF_{V1\rightarrow PM}$ $EPSCs_{sCRACM}$ in a pair of neighboring L5 PV (left) and Pyr (right) cells. (**b**) Heat map of EPSCs in ***6a*** superimposed with respective biocytin-filled L5 neurons. (**c**) Scatter plot, as previously described, of $EPSCs_{sCRACM}$ in PV and Pyr cell pairs in L5 $FF_{V1\rightarrow PM}$. The total current in PV and Pyr cells were not significantly different. (**d-f**) Similar data as in ***6a-c*** but for L5 $FF_{LM\rightarrow PM}$. (**g,h**) PV cell excitation, normalized to the excitation of a neighboring Pyr cell, is stronger in L2/3 than in L5 for both V1→PM (***g***) and LM→PM pathways (***h***). (**i**) Total EPSC in each row of the 8×16 grid normalized to total current recorded, plotted against row position (16 rows). Note that L5 PV cells do not show significant differences in the laminar distribution of EPSCs in the two pathways, but L5 Pyr cells receive more input in the upper layers from LM than from V1. (**j**) Interareal input in L2-4 for L5 PV cells (left) in PM is not significantly different for the two pathways. L5 Pyr cells (right) receive more L2-4 input in the $FF_{V1\rightarrow PM}$ than in the $FF_{LM\rightarrow PM}$ pathway. L2-4 input calculated as the average EPSC in each row that resided in L2-4, shown as the percentage of the total EPSC in the cell (***$p < 0.001$, Mann-Whitney U-test).

Figure 6. FB input to L5 neurons. (**a**) $FB_{PM\rightarrow LM}$ $EPSCs_{sCRACM}$ in a pair of neighboring L5 PV (left) and Pyr (right) cells. (**b**) Heat map of EPSCs from ***7a*** superimposed with the respective biocytin-filled L5 neurons. (**c**) Scatter plot of all L5 PV-Pyr neuron pairs receiving input from $FB_{PM\rightarrow LM}$. Total EPSC in the two cell types are not significantly different. (**d-f**) Similar data as ***7a-c*** but for the $FB_{PM\rightarrow V1}$ pathway. (**g**) Total EPSC in each row of the stimulation grid plotted against row position. The grids of the two different pathways are aligned to pial surface. (**h**) EPSCs in PV cells normalized to EPSCs in neighboring Pyr cells ($EPSC_{PV}/EPSC_{Pyr}$) for all L5 pathways arranged from most FF to most FB. Unlike in L2/3, the $EPSC_{PV}/EPSC_{Pyr}$ ratios in L5 are not significantly different in different pathways ($p > 0.2$, Kruskal-Wallis test). Red boxes describe data from Yang et al., 2013. (**i**) Interareal EPSCs are faster in PV than in Pyr cells in all L5 pathways (*$p < 0.05$, ***$p < 0.001$, paired t-test).

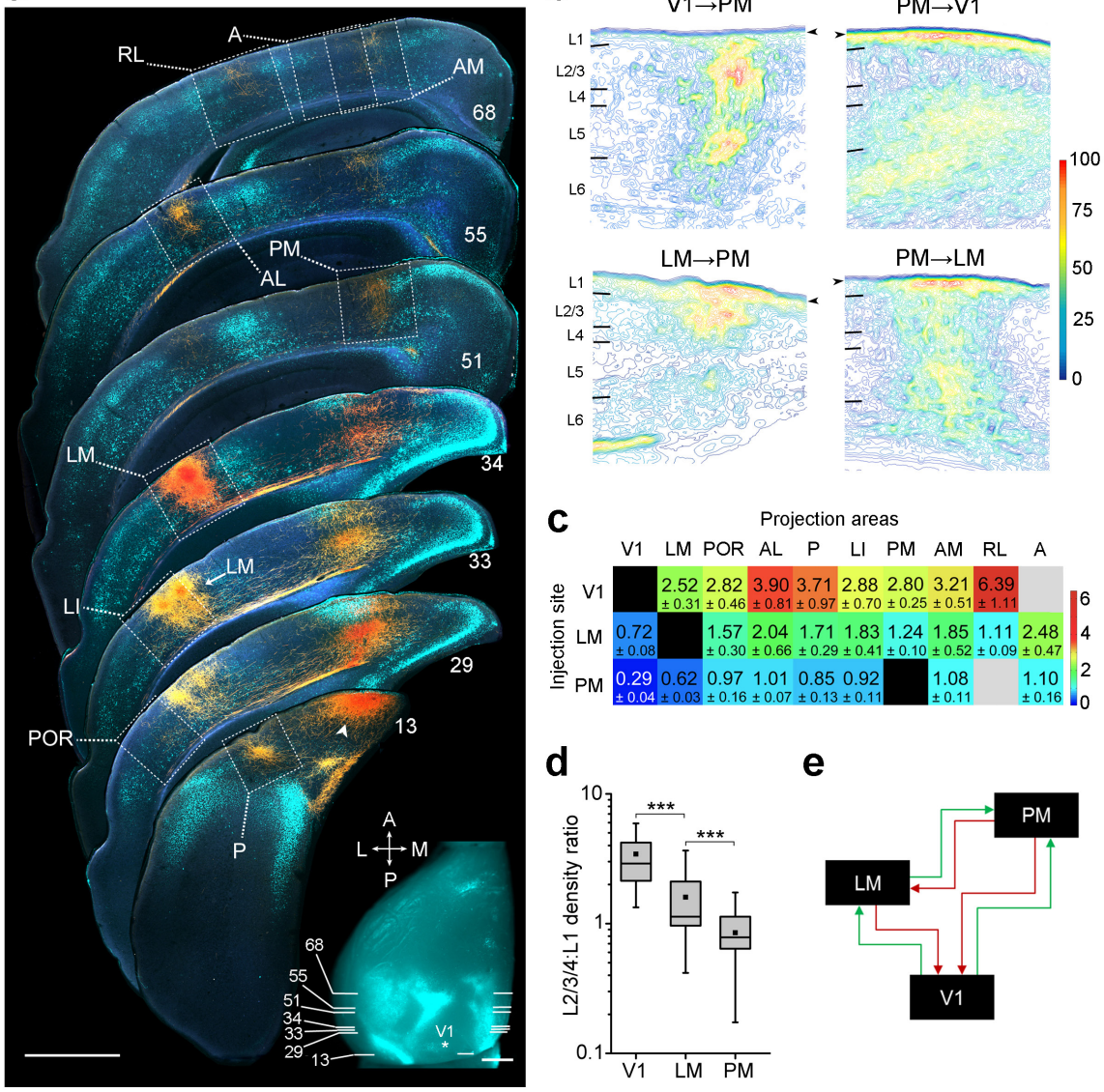
a
RL
A
AM
68
55
PM
AL
51
LM
34
LM
33
LI
29
POR
13
P
A
L
M
P
68
55
51
34
33
29
13
V1
b
V1→PM
PM→V1
LM→PM
PM→LM
L1
L2/3
L4
L5
L6
100
75
50
25
0
c
Projection areas
V1 LM POR AL P LI PM AM RL A
Injection site
V1 2.52 ± 0.31 2.82 ± 0.46 3.90 ± 0.81 3.71 ± 0.97 2.88 ± 0.70 2.80 ± 0.25 3.21 ± 0.51 6.39 ± 1.11
LM 0.72 ± 0.08 1.57 ± 0.30 2.04 ± 0.66 1.71 ± 0.29 1.83 ± 0.41 1.24 ± 0.10 1.85 ± 0.52 1.11 ± 0.09 2.48 ± 0.47
PM 0.29 ± 0.04 0.62 ± 0.03 0.97 ± 0.16 1.01 ± 0.07 0.85 ± 0.13 0.92 ± 0.11 1.08 ± 0.11 1.10 ± 0.16
6
4
2
0
d
L2/3/4:L1 density ratio
10
1
0.1
***
***
V1
LM
PM
e
PM
LM
V1

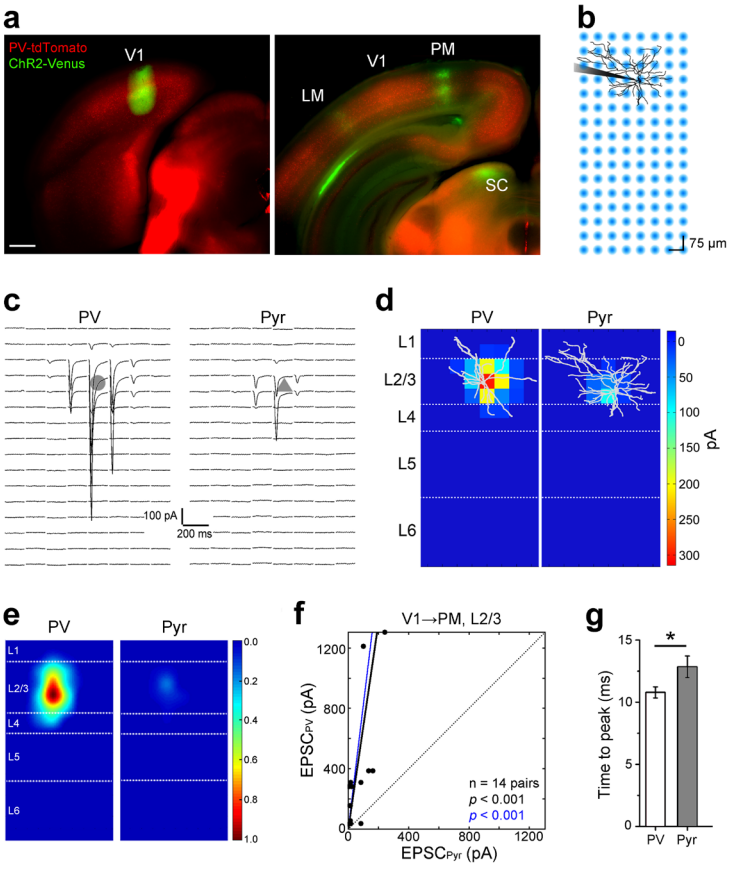
a
PV-tdTomato
ChR2-Venus
V1
V1
PM
LM
SC
b
75 µm
c
PV
Pyr
100 pA
200 ms
d
PV
Pyr
L1
L2/3
L4
L5
L6
0
50
100
150
200
250
300
pA
e
PV
Pyr
L1
L2/3
L4
L5
L6
0.0
0.2
0.4
0.6
0.8
1.0
f
V1→PM, L2/3
EPSCPV (pA)
EPSCPyr (pA)
0
400
800
1200
n = 14 pairs
p < 0.001
p < 0.001
g
Time to peak (ms)
0
5
10
15
*
PV
Pyr

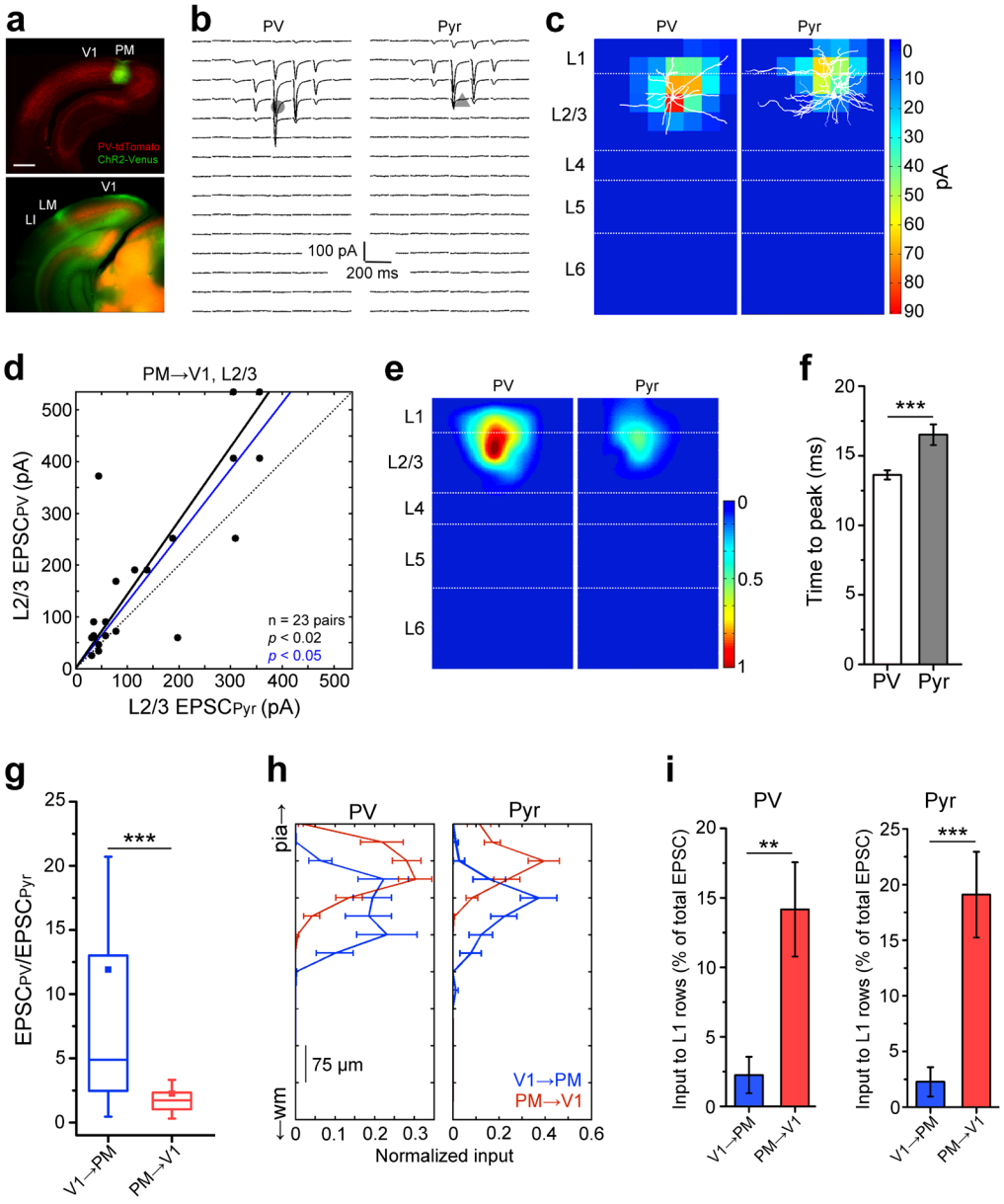
a
V1
PM
PV-tdTomato
ChR2-Venus
V1
LM
LI
b
PV
Pyr
100 pA
200 ms
c
PV
Pyr
L1
L2/3
L4
L5
L6
0
10
20
30
40
50
60
70
80
90
pA
d
PM→V1, L2/3
L2/3 EPSCPV (pA)
L2/3 EPSCPyr (pA)
n = 23 pairs
p < 0.02
p < 0.05
e
PV
Pyr
L1
L2/3
L4
L5
L6
0
0.5
1
f
Time to peak (ms)
***
PV
Pyr
g
EPSCPV/EPSCPyr
***
V1→PM
PM→V1
h
PV
Pyr
pia
wm
75 µm
V1→PM
PM→V1
Normalized input
i
PV
Pyr
Input to L1 rows (% of total EPSC)
**
***
V1→PM
PM→V1

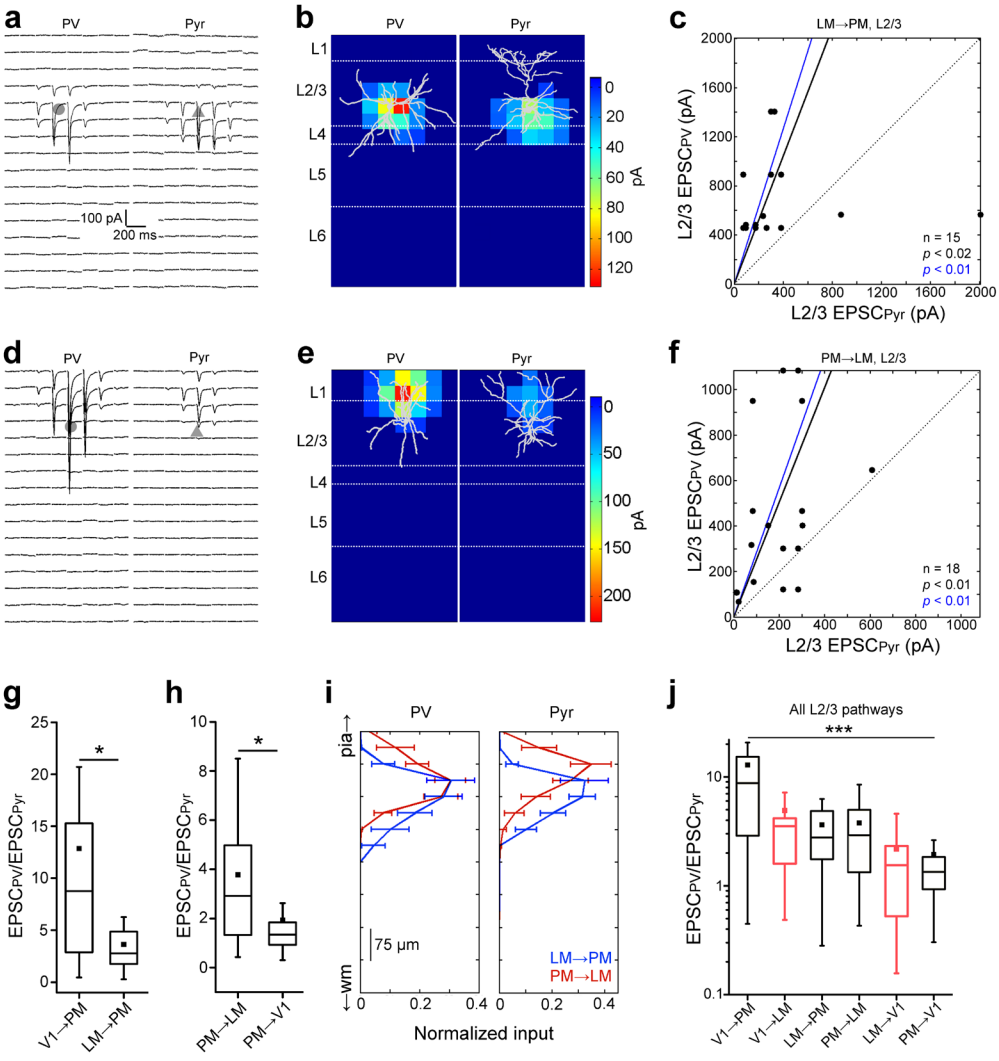
a
PV
Pyr
100 pA
200 ms
b
PV
Pyr
L1
L2/3
L4
L5
L6
0
20
40
60
80
100
120
pA
c
LM→PM, L2/3
L2/3 EPSCPV (pA)
L2/3 EPSCPyr (pA)
n = 15
p < 0.02
p < 0.01
d
PV
Pyr
e
PV
Pyr
L1
L2/3
L4
L5
L6
0
50
100
150
200
pA
f
PM→LM, L2/3
L2/3 EPSCPV (pA)
L2/3 EPSCPyr (pA)
n = 18
p < 0.01
p < 0.01
g
EPSCPV/EPSCPyr
*
V1→PM
LM→PM
h
EPSCPV/EPSCPyr
*
PM→LM
PM→V1
i
PV
Pyr
pia
wm
75 µm
LM→PM
PM→LM
Normalized input
j
All L2/3 pathways
***
EPSCPV/EPSCPyr
V1→PM
V1→LM
LM→PM
PM→LM
LM→V1
PM→V1

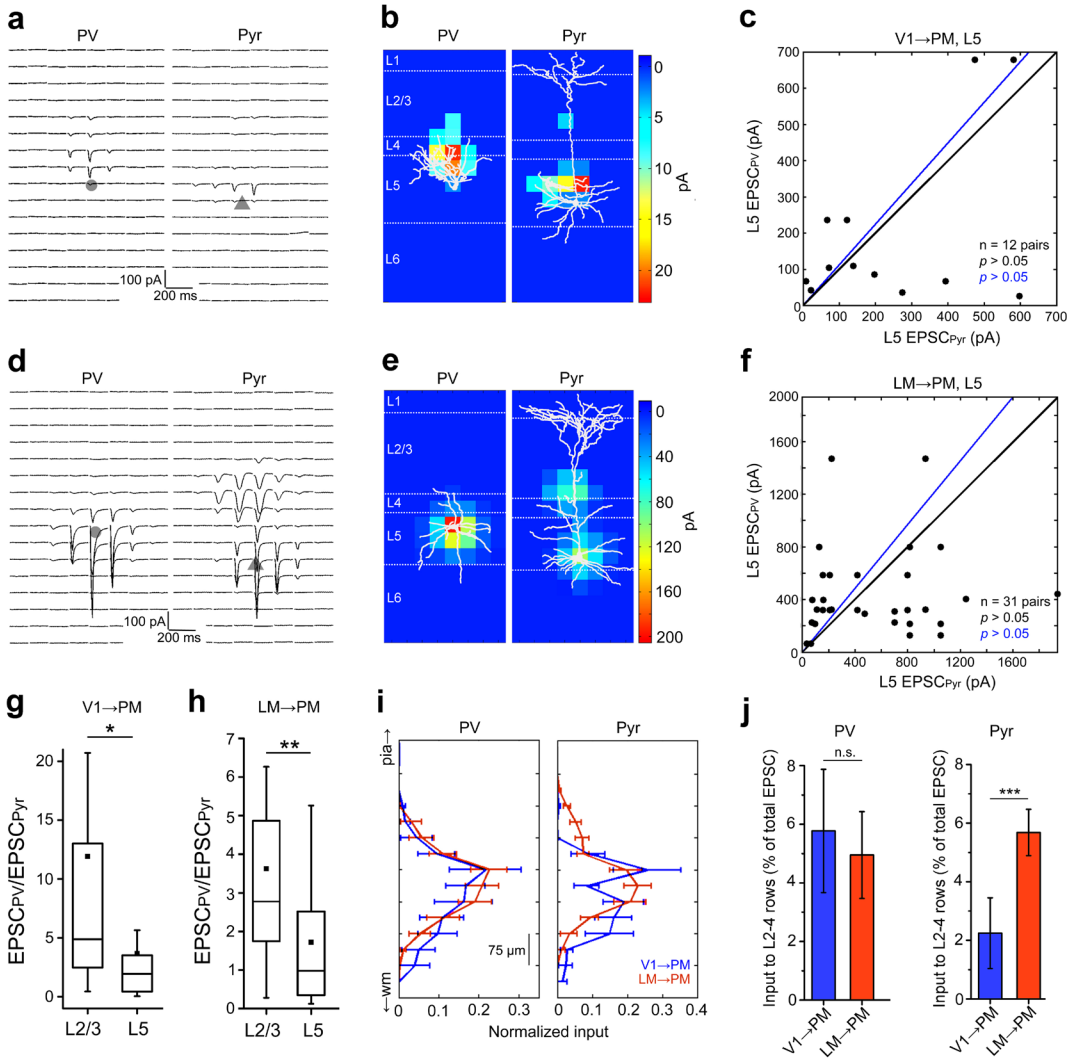
a
PV
Pyr
100 pA
200 ms
b
PV
Pyr
L1
L2/3
L4
L5
L6
0
5
10
15
20
pA
c
V1→PM, L5
L5 EPSCPV (pA)
L5 EPSCPyr (pA)
n = 12 pairs
p > 0.05
p > 0.05
d
PV
Pyr
100 pA
200 ms
e
PV
Pyr
L1
L2/3
L4
L5
L6
0
40
80
120
160
200
pA
f
LM→PM, L5
L5 EPSCPV (pA)
L5 EPSCPyr (pA)
n = 31 pairs
p > 0.05
p > 0.05
g
V1→PM
*
EPSCPV/EPSCPyr
L2/3
L5
h
LM→PM
**
EPSCPV/EPSCPyr
L2/3
L5
i
PV
Pyr
pia→
←wm
75 µm
V1→PM
LM→PM
Normalized input
j
PV
n.s.
Input to L2-4 rows (% of total EPSC)
V1→PM
LM→PM
Pyr
***
Input to L2-4 rows (% of total EPSC)
V1→PM
LM→PM

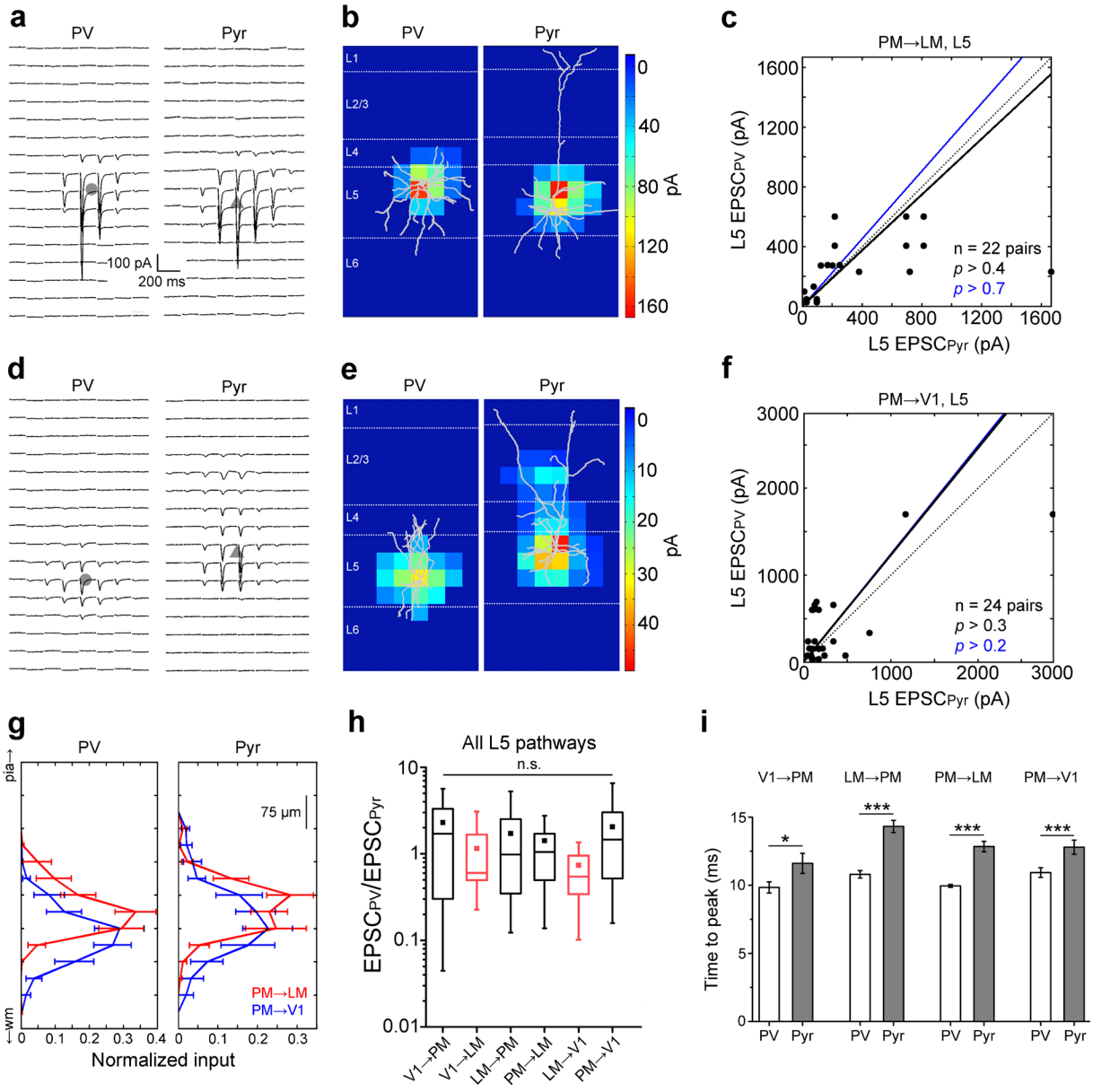
a
PV
Pyr
100 pA
200 ms
b
PV
Pyr
L1
L2/3
L4
L5
L6
0
40
80
120
160
pA
c
PM→LM, L5
L5 EPSCPV (pA)
L5 EPSCPyr (pA)
n = 22 pairs
p > 0.4
p > 0.7
d
PV
Pyr
e
PV
Pyr
L1
L2/3
L4
L5
L6
0
10
20
30
40
pA
f
PM→V1, L5
L5 EPSCPV (pA)
L5 EPSCPyr (pA)
n = 24 pairs
p > 0.3
p > 0.2
g
PV
Pyr
pia→
←wm
75 µm
PM→LM
PM→V1
Normalized input
h
All L5 pathways
n.s.
EPSCPV/EPSCPyr
V1→PM
V1→LM
LM→PM
PM→LM
LM→V1
PM→V1
i
V1→PM
LM→PM
PM→LM
PM→V1
Time to peak (ms)
PV
Pyr

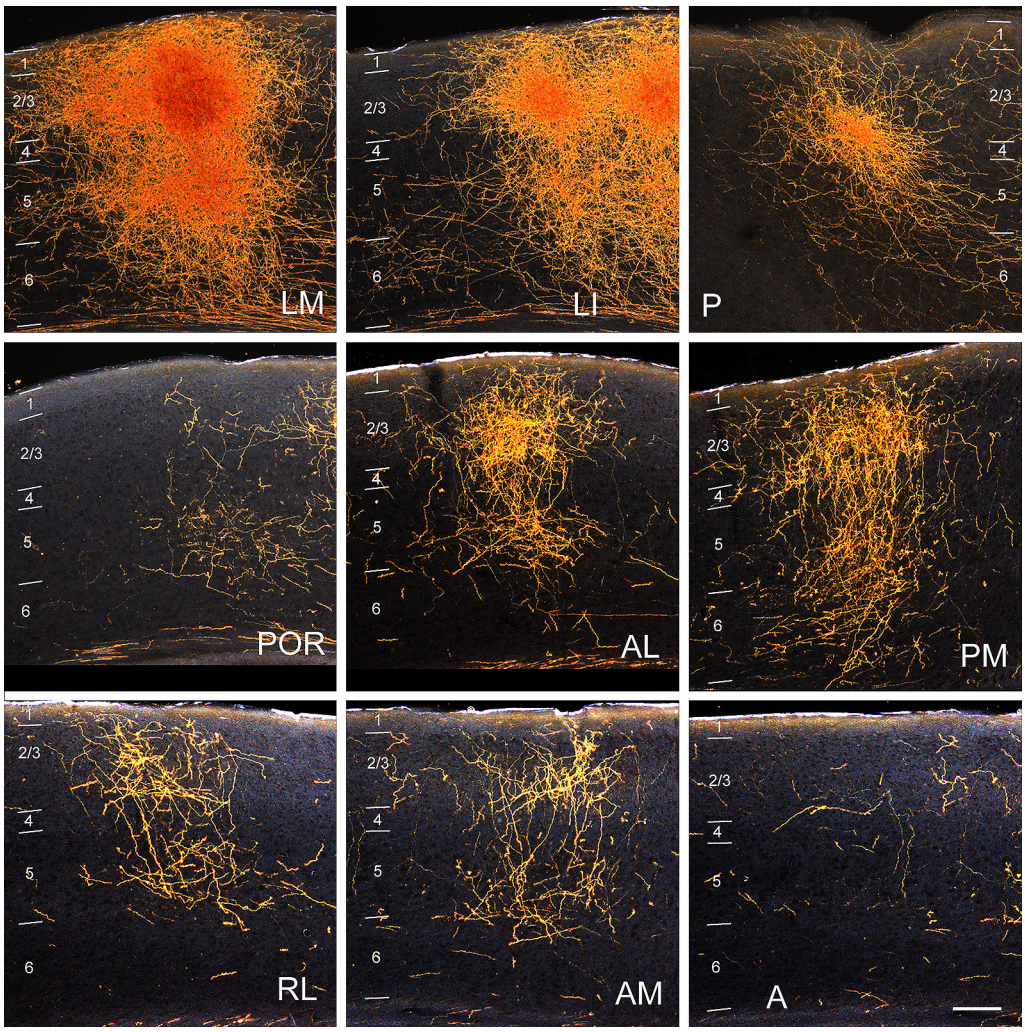
1
2/3
4
5
6
LM
LI
P
POR
AL
PM
RL
AM
A

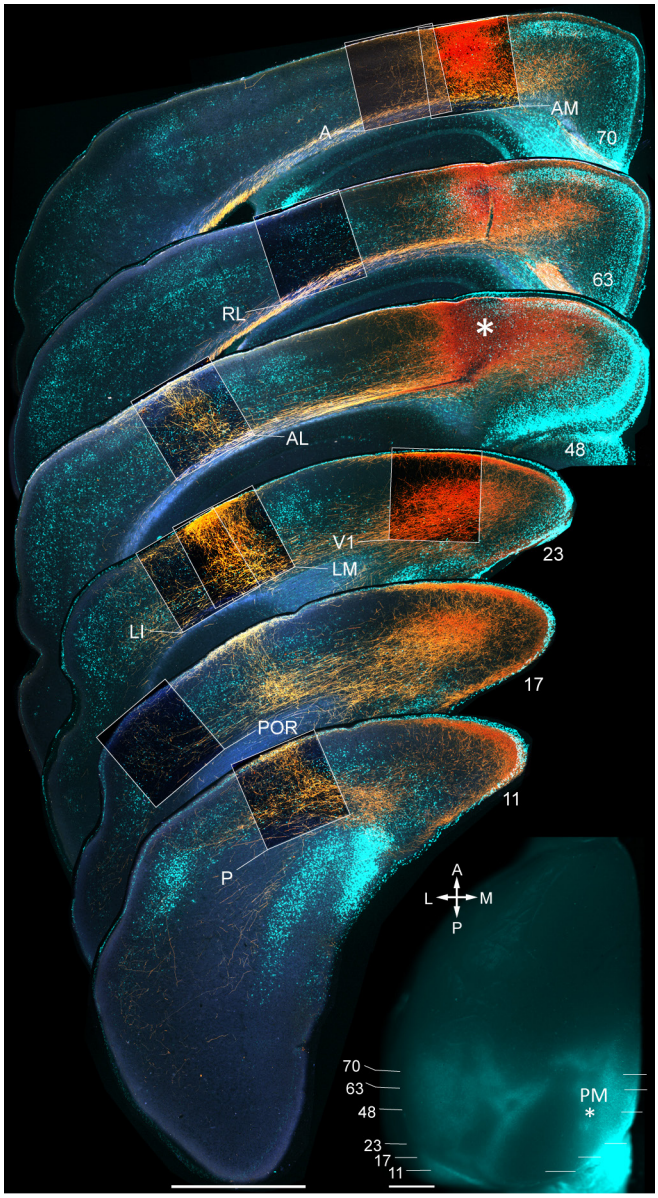
A
AM
70
63
RL
*
AL
48
V1
LM
23
LI
17
POR
11
P
A
L
M
P
70
63
48
23
17
11
PM
*

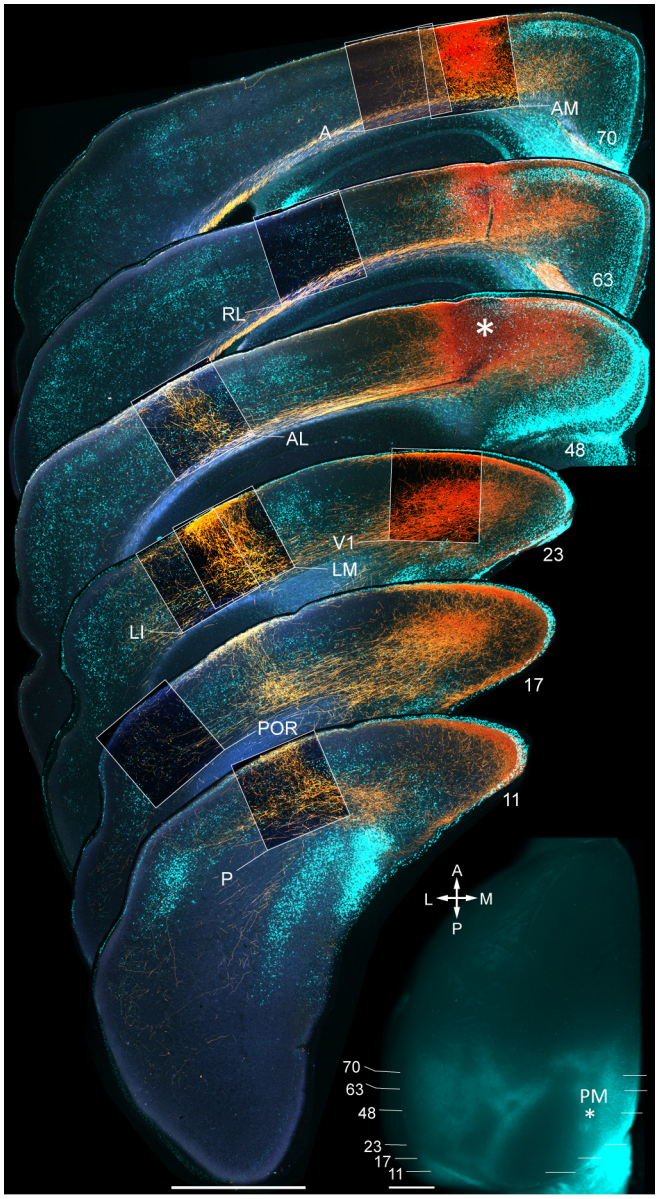
AM
A
70
63
RL
*
AL
48
V1
LM
23
LI
17
POR
11
P
A
L
M
P
70
63
48
23
17
11
PM
*

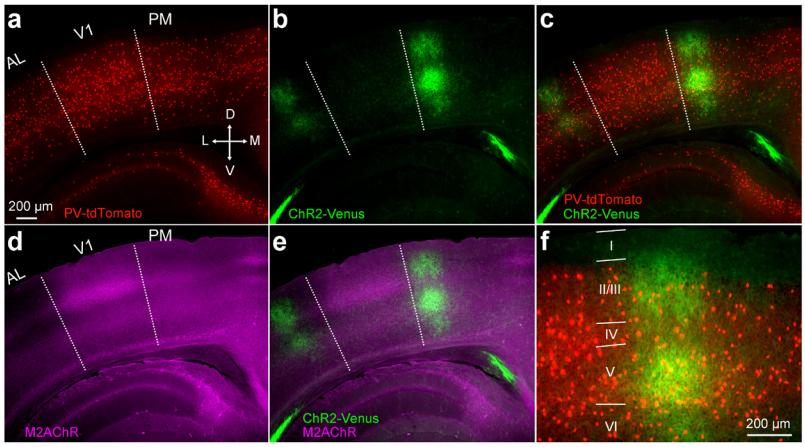
a
V1
PM
AL
D
L
M
V
200 µm
PV-tdTomato
b
ChR2-Venus
c
PV-tdTomato
ChR2-Venus
d
V1
PM
AL
M2AChR
e
ChR2-Venus
M2AChR
f
I
II/III
IV
V
VI
200 µm

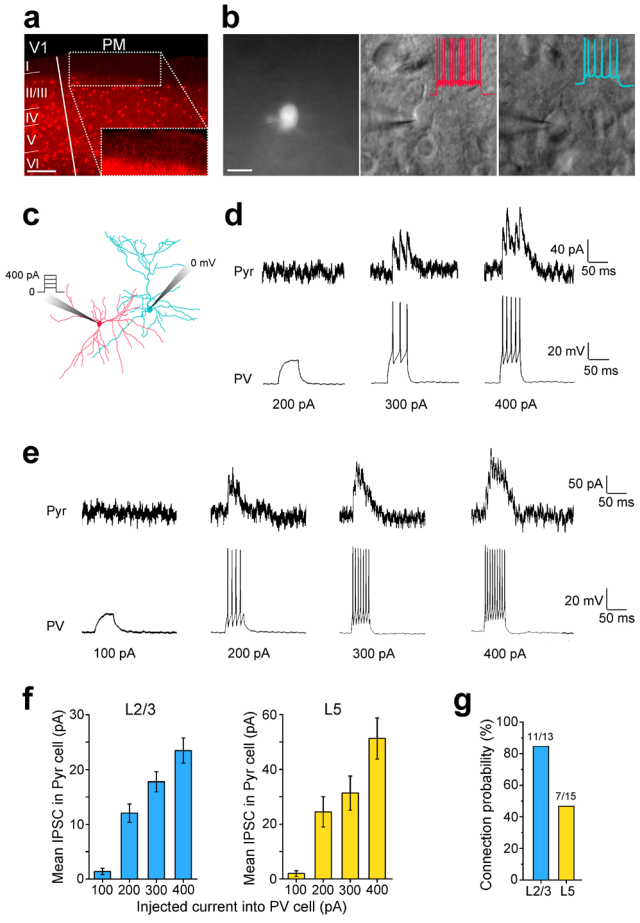
a
V1
PM
I
II/III
IV
V
VI
b
c
400 pA
0
0 mV
d
Pyr
PV
40 pA
50 ms
20 mV
50 ms
200 pA
300 pA
400 pA
e
Pyr
PV
50 pA
50 ms
20 mV
50 ms
100 pA
200 pA
300 pA
400 pA
f
L2/3
L5
Mean IPSC in Pyr cell (pA)
Injected current into PV cell (pA)
100 200 300 400
g
Connection probability (%)
11/13
7/15
L2/3 L5

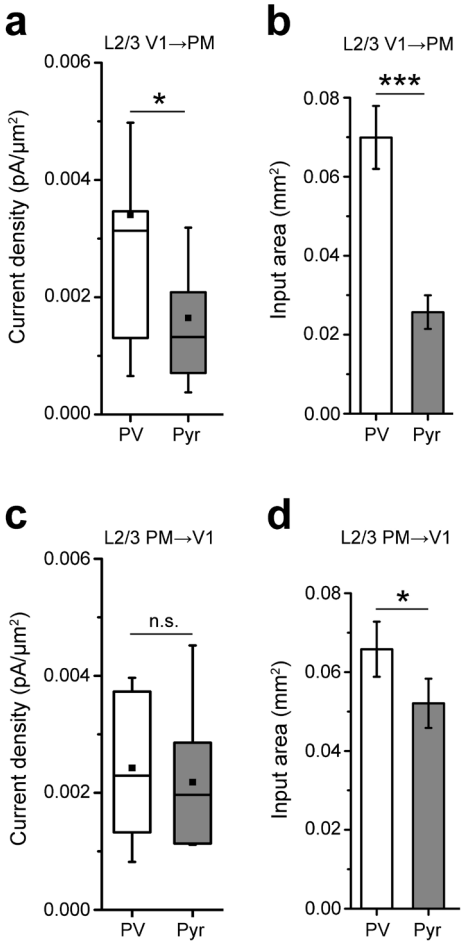
a
L2/3 V1→PM
Current density (pA/μm²)
0.006
0.004
0.002
0.000
*
PV
Pyr
b
L2/3 V1→PM
Input area (mm²)
0.08
0.06
0.04
0.02
0.00
***
PV
Pyr
c
L2/3 PM→V1
Current density (pA/μm²)
0.006
0.004
0.002
0.000
n.s.
PV
Pyr
d
L2/3 PM→V1
Input area (mm²)
0.08
0.06
0.04
0.02
0.00
*
PV
Pyr

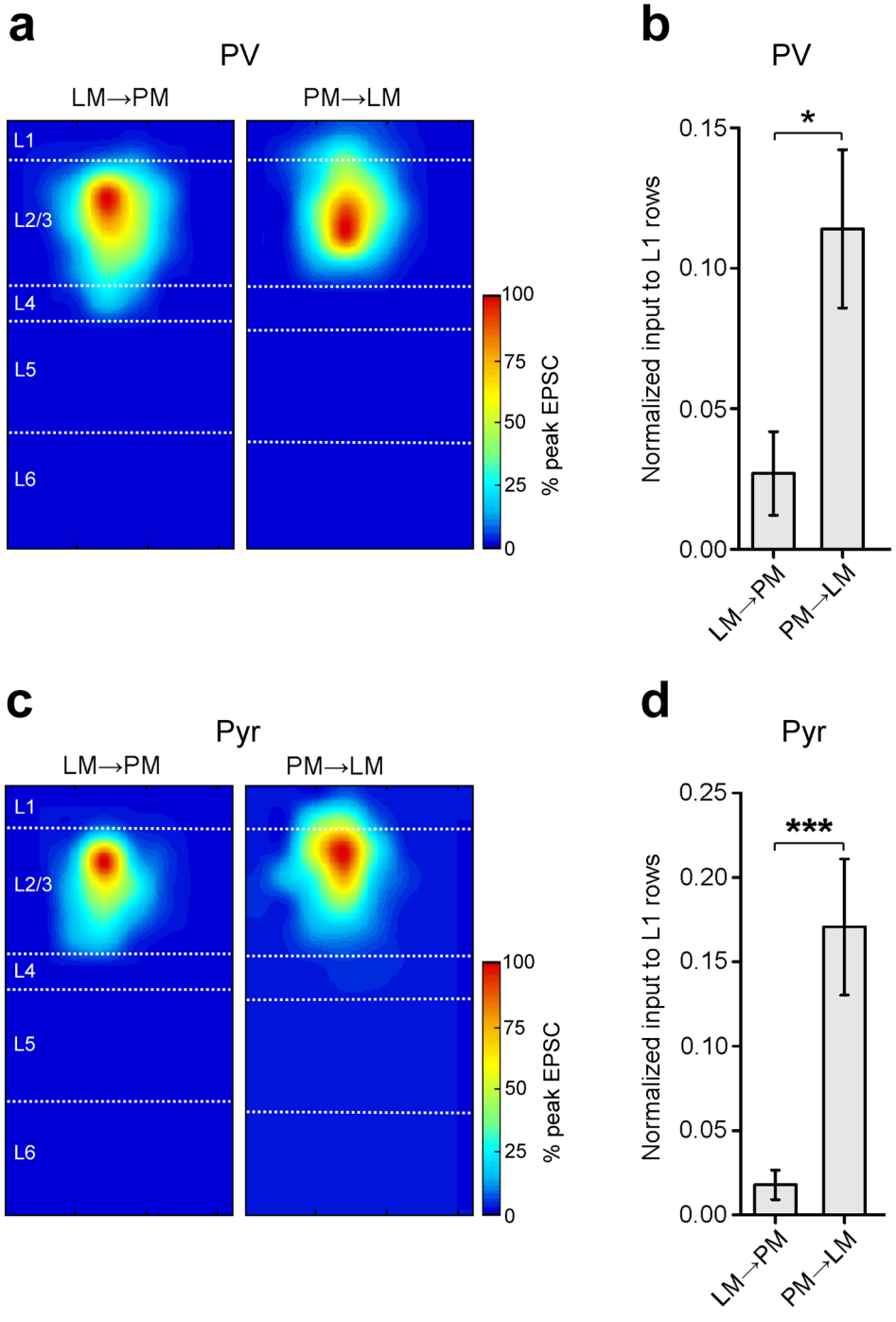
a
PV
LM→PM
PM→LM
L1
L2/3
L4
L5
L6
100
75
50
25
0
% peak EPSC
b
PV
Normalized input to L1 rows
0.15
0.10
0.05
0.00
*
LM→PM
PM→LM
c
Pyr
LM→PM
PM→LM
L1
L2/3
L4
L5
L6
100
75
50
25
0
% peak EPSC
d
Pyr
Normalized input to L1 rows
0.25
0.20
0.15
0.10
0.05
0.00
***
LM→PM
PM→LM

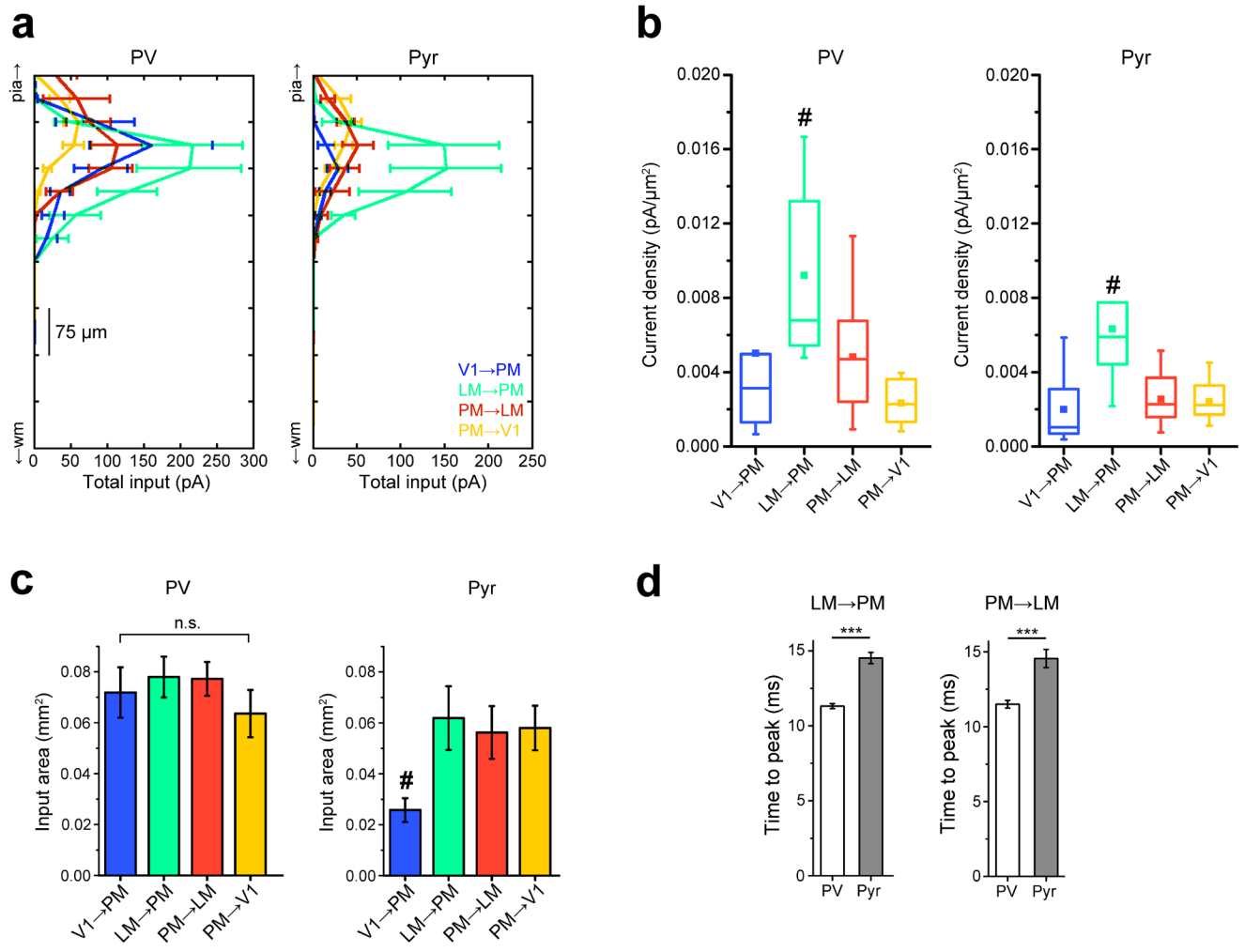
a
PV
Pyr
pia→
←wm
75 μm
0 50 100 150 200 250 300
0 50 100 150 200 250
Total input (pA)
V1→PM
LM→PM
PM→LM
PM→V1
b
PV
Pyr
Current density (pA/μm²)
0.020
0.016
0.012
0.008
0.004
0.000
#
V1→PM
LM→PM
PM→LM
PM→V1
c
PV
Pyr
n.s.
Input area (mm²)
0.08
0.06
0.04
0.02
0.00
#
V1→PM
LM→PM
PM→LM
PM→V1
d
LM→PM
PM→LM
***
Time to peak (ms)
15
10
5
0
PV
Pyr